water

MDPI

Article

Heterojunction-Based Photocatalytic Degradation of Rose Bengal Dye via Gold-Decorated α-Fe_2O_3-CeO_2 Nanocomposites under Visible-Light Irradiation

Najah Ayad Alshammari [1,2], Samia Abdulhammed Kosa [1], Rajan Patel [3] and Maqsood Ahmad Malik [4,*]

[1] Department of Chemistry, Faculty of Sciences, King Abdulaziz University (KAU), Jeddah 21589, Saudi Arabia; skousah@kau.edu.sa (S.A.K.)
[2] Department of Chemistry, Faculty of Sciences, Northern Border University (NBU), Arar 91431, Saudi Arabia
[3] Biophysical Chemistry Laboratory, Centre for Interdisciplinary Research in Basic Sciences, Jamia Millia Islamia, New Delhi 110025, India; rpatel@jmi.ac.in
[4] Department of Chemistry, Faculty of Sciences, Jamia Millia Islamia, New Delhi 110025, India
* Correspondence: mamalik@jmi.ac.in

Abstract: Developing photocatalytic nanomaterials with unique physical and chemical features using low-cost and eco-friendly synthetic methods is highly desirable in wastewater treatment. In this work, the magnetically separable α-Fe_2O_3-CeO_2 nanocomposite (NC), with its respective metal oxides of α-Fe_2O_3 and CeO_2 nanoparticles, was synthesized using a combination of hexadecyltrimethylammonium bromide (CATB) and ascorbic acid via the hydrothermal method. To tune the band gap, the heterojunction nanocomposite of α-Fe_2O_3-CeO_2 was decorated with plasmonic Au nanoparticles (Au NPs). The various characterization methods, such as FTIR, UV-vis DRS, XRD, XPS, TEM, EDX, SEM, and PL, were used to determine the properties of the materials, including their morphology, elemental composition, optical properties, band gap energy, and crystalline phase. The nanocomposite of α-Fe_2O_3-CeO_2@Au was utilized to remove Rose Bengal (RB) dye from wastewater using a photocatalytic technique when exposed to visible light. A comprehensive investigation of the impact of the catalyst concentration and initial dye concentration was conducted to establish the optimal photodegradation conditions. The maximum photocatalytic efficiency of α-Fe_2O_3-CeO_2@Au (50 mg L^{-1}) for RB (20 ppm) dye removal was found to be 88.9% in 120 min under visible-light irradiation at a neutral pH of 7 and 30 °C. Various scavengers, such as benzoquinone (BQ; 0.5 mM), tert-butyl alcohol (TBA; 0.5 mM), and ethylenediaminetetraacetic acid (EDTA; 0.5 mM), were used to investigate the effects of different free radicals on the photocatalytic process. Furthermore, the reusability of the α-Fe_2O_3-CeO_2@Au photocatalyst has also been explored. Furthermore, the investigation of the potential mechanism demonstrated that the heterojunction formed between α-Fe_2O_3 and CeO_2, in combination with the presence of deposited Au NPs, led to an enhanced photocatalytic efficiency by effectively separating the photogenerated electron (e^-)–hole (h^+) pairs.

Keywords: nanocomposite; heterojunction; surface functionalization; photocatalysis

check for updates

Citation: Alshammari, N.A.; Kosa, S.A.; Patel, R.; Malik, M.A. Heterojunction-Based Photocatalytic Degradation of Rose Bengal Dye via Gold-Decorated α-Fe_2O_3-CeO_2 Nanocomposites under Visible-Light Irradiation. *Water* **2024**, *16*, 1334. https://doi.org/10.3390/w16101334

Academic Editors: Chiara Lo Porto and Vincenza Armenise

Received: 2 April 2024
Revised: 25 April 2024
Accepted: 29 April 2024
Published: 8 May 2024

Copyright: © 2024 by the authors. Licensee MDPI, Basel, Switzerland. This article is an open access article distributed under the terms and conditions of the Creative Commons Attribution (CC BY) license (https://creativecommons.org/licenses/by/4.0/).

1. Introduction

The production of synthetic dyes, such as fabrics, papers, cosmetics, and leather, has increased in several industries [1,2]. Approximately 7×10^7 tons of these toxic dyes are manufactured annually [3], and often 5×10^3 tons are released into the aquatic environment as wastewater [4], posing a threat to human health and other living organisms [5,6]. One such dye is Rose Bengal (4,5,6,7-tetrachloro-2′,4′,5′,7′-tetraiodofluorescein), also recognized as Acid Red 94, a synthetic dye belonging to the basic xanthene group. Rose Bengal is water-soluble and comprises functional groups such as hydroxyl and carboxyl, along with aromatic rings crucial for its molecular interactions. It is widely employed in various industries, like textiles, cosmetics, medical diagnostics, and microbiology, as a staining agent.

However, its widespread use has resulted in its presence in wastewater effluents. Despite its utility, this dye is hazardous and capable of causing skin and eye irritation. If released into water bodies, it can pose a significant threat to aquatic ecosystems. Furthermore, it is not biodegradable, which makes it necessary to have effective strategies for its disposal and removal from wastewater. Fortunately, Rose Bengal is light-sensitive, particularly to visible and UV wavelengths, rendering it prone to photodegradation [7–12].

Researchers have tried to remove pollutants from wastewater using conventional methods such as adsorption [13–16], oxidation [17], biodegradation [18], and membrane [19], but they are both inefficient and expensive [8]. Therefore, there is a crucial demand for an affordable and environmentally friendly approach to treating dye wastewater before it is disposed of into the environment [19–22]. Photocatalysis is mainly used to degrade textile dyes using effective semiconductor photocatalysts [22,23]. The limited recombination rate of electron–hole pairs are responsible for efficient degradation upon solar or UV–visible-light excitation [21–23]. Semiconductor nanomaterials ranging from 1 to 100 nm have garnered significant interest in photocatalysis because of their distinct physical and chemical properties compared to bulk materials [22–24]. Among others, transition metal oxide and semiconductor nanomaterials are appealing candidates in the photolysis field [21–23] because of their biocompatibility, remarkable stability, and capacity to produce charge carriers when stimulated with sufficient light energy [23,24].

Chemical catalysis and energy conversion are two areas where intelligent and effective nanomaterials are gaining popularity. Nanostructured metal oxides, including CeO_2, Fe_2O_3, TiO_2, MnO_2, ZnO, Fe_3O_4, and SnO_2, have been used to drive chemical reactions instead of conventional energies [25–31]. Of these metal oxides, α-Fe_2O_3 is a semiconductor with great potential for the breakdown of organic contaminants through photocatalysis and the generation of hydrogen in water splitting because of its natural abundance, chemical stability, low band gap, and environmental friendliness [32,33]. Although possessing these characteristics, α-Fe_2O_3 exhibits a high recombination rate due to the short path length for hole diffusion and its restricted oxidation capability. This rapid recombination of electron–hole pairs hinders the commercial viability of the material. To address this issue, it is essential to incorporate additional active materials with a greater surface area in the host matrix [34].

Many researchers have created heterojunction composites, including α-Fe_2O_3@TiO_2, α-Fe_2O_3@ZnO, Fe_3O_4-ZnO/TiO_2, α-Fe_2O_3@SnO_2, Fe_3O_4-CdO, and TiO_2-CeO_2, in an attempt to harvest solar energy, reduce the charge carrier recombination rate, and increase the photocatalytic activity [35–40]. To improve electron–hole pair separation, rare-earth oxides can be combined with α-Fe_2O_3 [41]. Because of its ability to both gain and lose oxygen, the multifunctional rare-earth metal oxide CeO_2 is one of several oxides of rare-earth metals that could be used in photocatalysis. The narrow band gap and oxidative–reductive capability of the Ce(III)/Ce(IV) pair make CeO_2 an attractive photocatalytic candidate [42]. An increase in photocatalytic activity can be achieved through the reversible transformation of Ce(III)/Ce(IV) couples, which allows for the movement of electrons and the diffusion of charge carriers between CeO_2 and other semiconductors, like TiO_2, MoS_2, and CdS [43–45]. Thus, creating a heterojunction of Fe_2O_3 with CeO_2 makes sense, has also enhanced the redox stability of the material, and is essential for photocatalytic performance. Numerous scientists have developed heterojunction composites comprising Fe_2O_3 and CeO_2 to explore their potential in various applications, such as photocatalytic hydrogen evolution, ethanol conversion, supercapacitor technology, and dye degradation [46–49].

Moreover, researchers have observed that covering the surface of NPs with noble metals like platinum, silver, or gold can further enhance their electron–hole separation and photocatalytic activity [50–52]. The surface plasmon resonance (SPR) effects of these nanoparticles can considerably promote the ability of photocatalysts to respond to visible light [50–52]. Gold nanoparticles, in particular, are highly stable, with enhanced visible-light absorption and efficient charge separation, and can serve as an electron intermediary during

charge transfer, significantly preventing the recombination of photogenerated electron–hole pairs [53,54].

In this study, a hydrothermal method was used to fabricate CeO_2, α-Fe_2O_3, and the heterojunction of α-Fe_2O_3-CeO_2 nanoparticles combining different materials (CTAB and ascorbic acid) for surface modification to achieve improved physical and chemical properties [55,56]. CTAB is frequently utilized as a template to enhance uniformity and create a mesoporous structure [57,58], while ascorbic acid, with its four hydroxyl groups, functions as a ligand for metal oxide nanoparticles [59]. The visible-light absorption and decreased e^--h+ pair recombination improved with the decoration of Au NPs on the surface of α-Fe_2O_3-CeO_2 NC.

Gold ions were effectively transformed into nanoparticles by utilizing jujube extract as a reducing agent [60–62]. The α-Fe_2O_3-CeO_2@Au nanocomposite was designed to degrade RB dye, aiming to minimize the production of harmful byproducts and secondary pollution, in line with the sustainability goals [63]. The degradation was achieved under visible light. This light is a significant portion of solar radiation, making it a great source of renewable energy and reducing energy consumption compared to UV light [64]. The reusability capabilities of the as-synthesized photocatalyst were investigated to remove RB. A proposed mechanism for a photocatalytic process driven by visible light was also presented.

2. Materials and Methods

2.1. Materials

The reagents used in this study include iron(III) nitrate nonahydrate ($Fe_3(NO_3)_3.9H_2O$, purity 98.0%), cerium(III) nitrate ($Ce(NO_3)_3.\ 6H_2O$, purity 99.0%), Hexadecyltrimethylammonium bromide ($C_{19}H_{42}BrN$; purity 99.0%), L-ascorbic acid ($C_6H_8O_6$; purity 99.0%), Ethanol, (C_2H_5OH; Purity 99.5%), Ammonia (NH_3; purity 99.0%), Gold(III) chloride ($AuCl_3$; purity 99.0%), and Rose Bengal dye ($C_{20}H_2Cl_4I_4Na_2O_5$; purity 95.0%) were acquired from Sigma-Aldrich, St. Louis, MO, USA. Ziziphus jujuba fruit was purchased from the local market. All chemicals were utilized as received without additional purification. All of the solutions were prepared using deionized water.

2.2. Synthesis of Fe_2O_3, CeO_2, Fe_2O_3-CeO_2 and Fe_2O_3-CeO_2@Au NPs

For the preparation of Fe_2O_3 and CeO_2 NPs, a hydrothermal approach was carried out [65,66]. Initially, 2 g of $Fe(NO_3)_3{\cdot}9H_2O$ and $Ce(NO_3)_3.{\cdot}6H_2O$ were separately dissolved in 50 mL of deionized water to create a homogeneous solution. An aqueous solution of CTAB (10 mL, 0.2 M) and ascorbic acid (20 mL, 1.0 M) was added to each metal ion solution with continuous stirring at 50 °C. After that, aqueous ammonia was slowly added, drop by drop, to the reaction mixture, until a pH of 12 was achieved [67,68]. The mixture was moved into a Teflon-lined autoclave with a volume of 100 mL. Following that, it was subjected to heating at 180 °C in the oven for a period of 24 h. The obtained material was centrifuged at 4000 rpm for 20 min and rinsed multiple times with deionized water and ethanol. The obtained solid samples were subjected to drying at a temperature of 70 °C for a duration of 24 h, and subsequently subjected to calcination at a temperature of 500 °C for a duration of four hours.

Furthermore, α-Fe_2O_3-CeO_2 NC was prepared by mixing an equal quantity of metal ion solutions of $Fe(NO_3)_3{\cdot}9H_2O$ and $Ce(NO_3)_3{\cdot}6H_2O$ in one beaker and an aqueous solution of 10 mL CTAB (0.2 M) and 20 mL ascorbic acid (1.0 M) were added with continuous stirring at 50 °C. Aqueous ammonia was slowly added, drop by drop, to this mixture until the pH reached approximately 12. The mixture was moved into a Teflon-lined autoclave and heated at 180 °C in the oven for a period of 24 h. After allowing the autoclave to cool down, the as-prepared material was collected by centrifugation for 20 min at 4000 rpm and subsequently washed with deionized water and ethanol, followed by drying at 70 °C for 24 h and calcination at 500 °C for 4 h.

All prepared samples were kept in an airtight, dark place for additional characterization and use. The Au-supported α-Fe_2O_3-CeO_2 NPs were prepared by facile green synthesis technique employing aqueous jujube fruit extract as both a reducing and capping agent [69,70]. Initially, 20 g of dried jujube fruit was washed several times with deionized water and then air-dried at room temperature. The completely dried jujube fruit was crushed into fine powder and boiled for 20 min in 250 mL of deionized water. After being cooled down, the aqueous extract was filtered and then kept in a refrigerator for future utilization. The Au NPs deposition on the surface of α-Fe_2O_3-CeO_2 NC was achieved by dispersing 1.0 g of α-Fe_2O_3-CeO_2 NC in 10 mL of deionized water and vigorously stirring for 30 min. To this suspension, 15 mL of 0.20 M $AuCl_3$ aqueous solution was added and, subsequently, 10 mL of the jujube aqueous extract was added with continuous stirring for 1 h at 40 °C. After the complete reduction of Au^{3+} to Au° on the surface of α-Fe_2O_3-CeO_2 NC, the solid samples were centrifuged at 4000 rpm for 10 min and rinsed multiple times with deionized water and ethanol. Subsequently, the sample was further dried at 70 °C for 24 h. Eventually, α-Fe_2O_3-CeO_2@Au NC was collected and kept for further study. The schematic representation for the synthesis of α-Fe_2O_3, CeO_2, α-Fe_2O_3-CeO_2, and α-Fe_2O_3-CeO_2@Au NPs is illustrated in Figure 1.

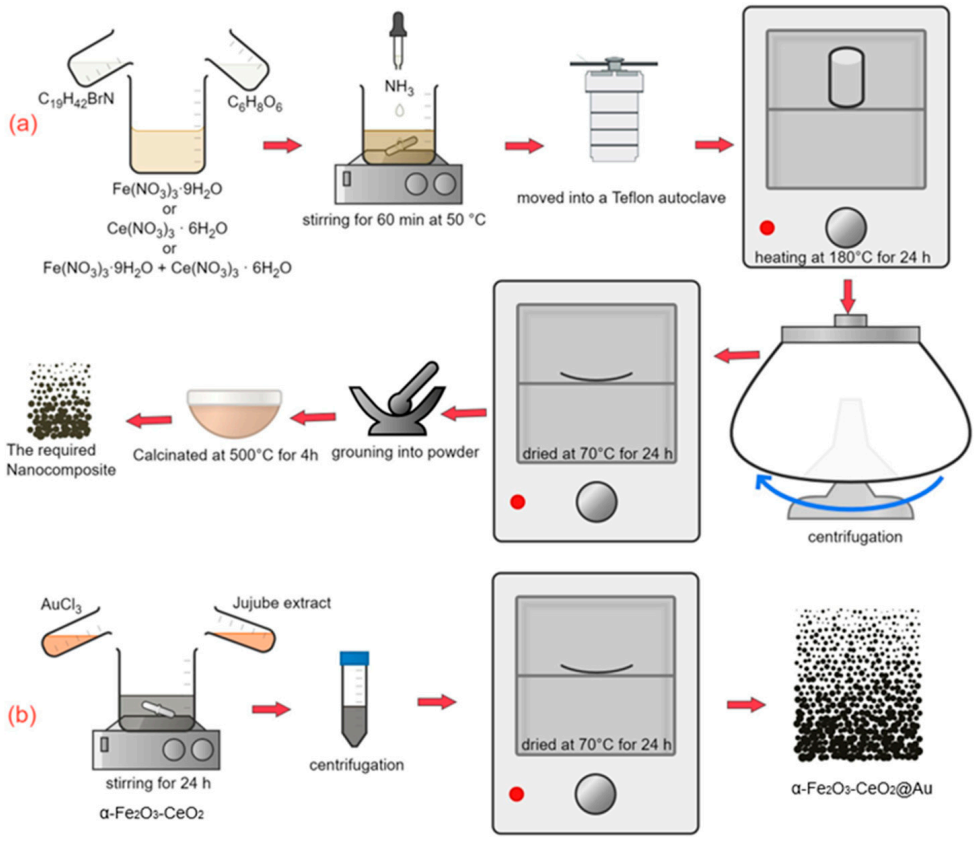

Figure 1. Synthesis representation showing the synthesis of (**a**) α-Fe_2O_3, CeO_2, α-Fe_2O_3-CeO_2, and (**b**) α-Fe_2O_3-CeO_2@Au.

2.3. Characterization

The surface morphology and elemental analysis of the prepared NPs were investigated by scanning electron microscopy (SEM) coupled with energy-dispersive X-ray spectrometry (EDS) (EDS Bruker, FEI Nova NanoSEM 450, Billerica, MA, USA). The determination of the sizes and shapes of the particles was carried out through the use of a transmission electron microscope (TEM) with Technai 200 model, which was produced by FEI and is based in Pleasanton, CA, USA. Fourier-transformed infrared spectra (FTIR) were also recorded in the range of 400–4000 cm^{-1} on Bruker Alpha-II spectrometer, Billerica, MA, USA, to verify

the essential function of functional groups in stabilizing, capping, and reducing during NP formation. Furthermore, Bruker D2 Phaser diffractometer, Billerica, MA, USA, was used to perform X-ray diffraction (XRD) analysis. The employed radiation was Cu Kα (1.5412 Å) over the 2θ range of 10–90°, with a step size of 0.002°, for the identification of photocatalysts' phases. X-ray photoelectron spectroscopy (XPS) was carried out to analyze the chemical and elemental composition of synthesized materials using Kratos Analytical AMICUS instrument, Manchester, United Kingdom, outfitted with a dual Al-Mg anode and an achromatic X-ray source (1468.6 eV), with a step of 0.1 eV. UV-vis DRS analysis was performed using Thermo Scientific Evolution 220 UV–visible spectrophotometer, Waltham, MA, USA, to acquire the absorption spectra of the as-prepared samples over a 200–900 nm range. The photoluminescence (PL) spectral analysis was performed using a fluorescence spectrophotometer LS 45, Perkin Elmer, Waltham, MA, USA).

2.4. Photocatalytic Activity

In this work, RB dye was utilized as the standard pollutant to examine the photocatalytic effectiveness of α-Fe_2O_3-CeO_2@Au NC. The dye was degraded in an aqueous media (deionized water) using a quartz photocatalytic double-layer reactor in the presence of visible irradiation. Before conducting photocatalytic degradation experiments, preliminary studies were carried out to determine the optimal concentration of the dye and a catalyst for their specific system. Each experiment used 50 mg L^{-1} of the photocatalyst, and an aqueous solution of RB (20 ppm) was used to disperse the sample in the dark for 30 min before irradiation to achieve adsorption–desorption equilibrium [49]. The reaction was conducted at a neutral pH of 7 [71,72] while maintaining the temperature at 30 °C using a circulating water-cooling system [73].

The photocatalyst was subsequently illuminated with visible light using a Tungsten lamp (400 W) under constant stirring. The concentration of the aqueous solution was determined using a UV-vis spectrophotometer at λ_{max} of 562 nm to monitor the decrease in the RB concentration over time. The α-Fe_2O_3-CeO_2@Au photocatalyst was then magnetically separated, washed, and dried for subsequent reactions to assess its stability and reusability. The photocatalytic experiments were optimized by varying photocatalyst and dye concentrations.

The data were also used to study the kinetic behavior of RB dye in the presence of the photocatalyst, and the rate constant (k) was calculated using Equation (1). The apparent rate constant of the reaction (k_{app}) in min^{-1} was acquired from the slope of the ln A_0/A_t Vs time plot.

$$\ln\left(\frac{A_0}{A_t}\right) = k_{app} \cdot t \quad (1)$$

Additionally, experiments were conducted to examine the effect of different free radicals on the photocatalytic process using various scavengers, including ethylenediaminetetraacetic acid (EDTA), tert-butyl alcohol (TBA), and benzoquinone (BQ), which were used as scavenging agents for h^+, $^{\bullet}OH$, and $^{\bullet}O_2^-$, respectively [49,74,75].

3. Results and Discussion

3.1. FTIR Spectroscopy Analysis

The synthesized NPs, α-Fe_2O_3, CeO_2, α-Fe_2O_3-CeO_2,, and α-Fe_2O_3-CeO_2@Au, were explored using the FTIR spectroscopic analysis, as shown in Figure 2. In general, the spectra did not substantially differ with the deposition of the Au NPs. The peaks of all samples at about 1630 cm^{-1} could be explained by the stretching and bending vibrations of O–H bonds in the absorbed molecular water. On the contrary, the stretching of O–H bonds in the hydroxyl groups of the capped ascorbic acid appeared as a broadband at around 3400 cm^{-1} [76]. Furthermore, the peaks located at 2800–2900 cm^{-1} could be correlated with the asymmetric and symmetric stretching of CH_2 in the methylene chains of amine, confirming that CTAB is coupled with the photocatalysts' surfaces [77]. Meanwhile, the bands corresponding to the C–H bending of the methyl group appeared at

approximately 1380 and 1460 cm^{-1} [76,78]. In addition, FTIR spectra at 1050–1160 cm^{-1} are associated with the C–O stretching vibration peaks that might refer to ester groups of ascorbic acid [79]. The observed peak intensities within the range of 1450–1700 cm^{-1}, 1462 cm^{-1}, and 1000–1250 cm^{-1} were attributed to the presence of C=O, C–H stretching vibrations, and C–N stretching due to phenolic acids, terpenoid-phenols, and aliphatic amines, respectively [80,81].

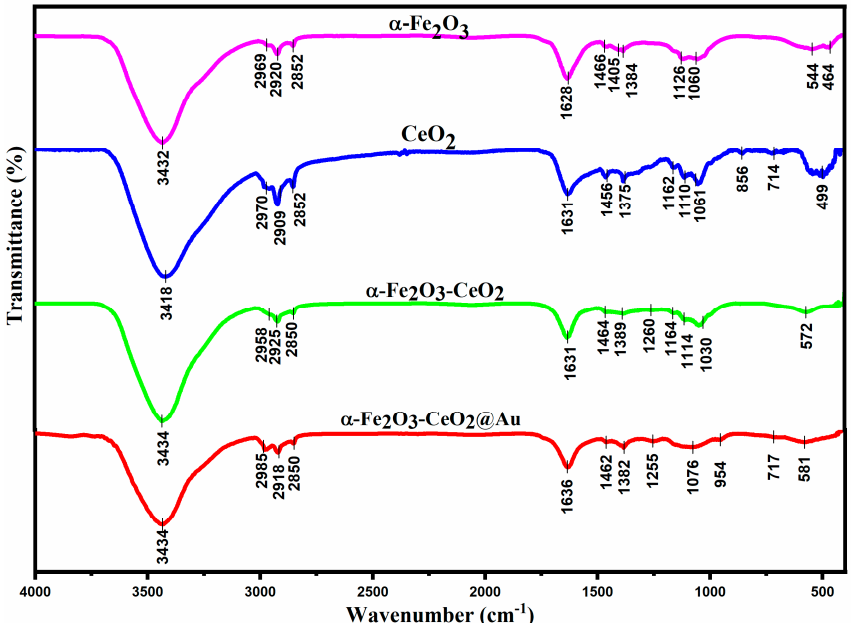

Figure 2. FTIR spectra of α-Fe_2O_3, CeO_2, α-Fe_2O_3-CeO_2, and α-Fe_2O_3-CeO_2@Au.

The prominent peaks at approximately 550 and 460 cm^{-1} were assigned to the bending and stretching vibrations of the Fe–O bonds [82], whereas the strong absorption bands at ~560 cm^{-1} were attributed to Ce–O. These results were consistent with the XRD, XPS, and EDX results, indicating the formation of CeO_2 and α-Fe_2O_3 NPs [78]. However, the peaks associated with Au NPs did not emerge in the α-Fe_2O_3-CeO_2@Au spectra. Similar observations were reported in a previous study [76]. This occurrence could be due to either the prominent bands of the supporting nanoparticles masking the weaker bands of the gold nanoparticles or the low concentration of gold nanoparticles in the photocatalysts [33]. Furthermore, ascorbic absorption signals at ≈1750–1760, specifically attributed to the stretching of the carbonyl group in the γ-lactone ring, did not emerge [83]. Overall, the shift in peak intensities towards higher (redshift) wavelengths assured the deposition of Au NPs on the synthesized photocatalysts.

3.2. UV–Visible DRS Analysis

DRS UV-visible absorption spectroscopy was used to investigate the light absorption properties of the synthesized materials, as shown in Figure 3. The absorption edge of pure CeO_2 NPs, as shown in Figure 3a, was around 490 nm in the UV region, proving the transition of electrons in the formed Ce–O bond [84]. Moreover, a strong absorption peak emerged at about 380 nm for CeO_2, referring to the charge transfer from O 2P to Ce 4f orbitals [85]. On the other hand, the UV-visible spectrum of pure α-Fe_2O_3 NPs represented a strong absorption band in the visible-light region (400–720 nm), which might enhance the use of visible light for photocatalysis [86]. The absorption peaks close to 200 nm were attributed to the direct transition of the metal oxide NPs [87]. Moreover, the broad peak at around 550 nm corresponded to the process of pair excitation in α-Fe_2O_3 NPs, while the one at approximately 650 nm might belong to the d–d transition [88,89].

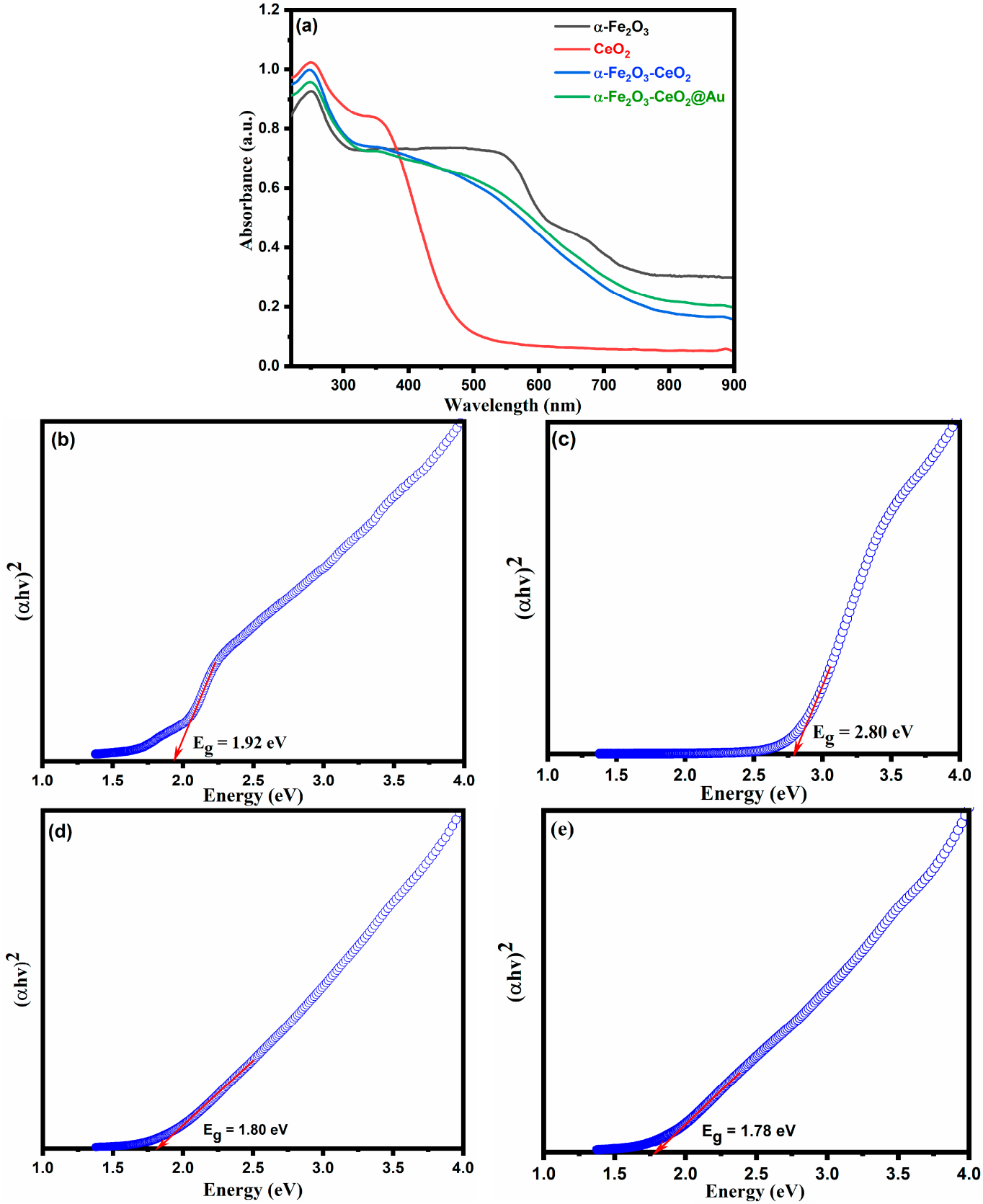

Figure 3. (**a**) UV–visible DRS spectra of as-synthesized samples and Band gap energy (E_g eV) of (**b**) α-Fe_2O_3, (**c**) CeO_2, (**d**) α-Fe_2O_3-CeO_2, and (**e**) α-Fe_2O_3-CeO_2@Au.

Compared to the individual metal oxide NPs, their NC exhibited a significant absorption ability under visible light irradiation. The strong absorption of visible light was linked to the significant amount of interfacial contact between CeO_2 and α-Fe_2O_3 NPs, forming a successful heterogeneous structure accountable for the UV–vis spectrum shifts and the bandgap width reduction [76]. Such an increase in the intensity might produce active electron–hole pairs, enhancing the photocatalytic efficiency [90,91]. In the case of Au-deposited α-Fe_2O_3-CeO_2, there was a slight gold band at around 520 nm, associated with the SPR effect; the band was not very prominent, and might overlap with the already existing broad peak of α-Fe_2O_3 at 530–570 nm. Furthermore, this could also be attributed to the comparatively minimal amount of Au NPs compared to the significant quantity of the support [92]. However, the deposition of Au NPs was confirmed with the results of XRD, XPS, and EDX [90]. The bandgaps were estimated for all samples from the carved edges of the Tauc plot by drawing ($\alpha h\upsilon$) against $h\upsilon$. It was found that the bandgaps of α-Fe_2O_3, CeO_2, α-Fe_2O_3-CeO_2, and α-Fe_2O_3-CeO_2@Au were 1.92 eV, 2.80 eV, 1.80 eV, and 1.78 eV, respectively, as represented in Figure 3b–e. Consequently, the NC band gap energy (Eg) was lower than its corresponding metal-oxide-based NPs', which was attributed to the formation of a heterojunction structure between α-Fe_2O_3 and CeO_2, which enhanced the surface electric charge and facilitated the transmission of photo-excited electrons [93]. Additionally, the difference in the bandgap of 0.02 eV for α-Fe_2O_3-CeO_2, after the gold deposition demonstrated the impact of the Au NPs on the photocatalyst's surface. These findings further supported the photocatalysts' catalytic activity in the visible-light region [94].

3.3. XRD Analysis

XRD analysis was used to investigate the crystal structure and purity of the as-prepared materials. Figure 4 shows the XRD patterns of α-Fe_2O_3, CeO_2, α-Fe_2O_3-CeO_2, and α-Fe_2O_3-CeO_2@Au nanoparticles. The XRD pattern of CeO_2 NPs shows characteristic peaks, observed at 28.6°, 33.2°, 47.6°, 56.6°, 59.4°, 69.8°, 76.9°, 79.3°, and 89.7°, corresponding to (111), (200), (220), (311), (222), (400), (331), (420), and (422) crystal planes, respectively. It can be inferred from the diffraction peaks that CeO_2 NPs possess a cubic fluorite structure and a face-centered cubic (FCC) structure and match well with the standard patterns of CeO_2 NPs (JCPDS-34-0394) [95]. The sharp diffraction peaks and the lack of additional peaks confirmed the high purity and crystallinity of the CeO_2 NPs [96]. The hematite phase (α-Fe_2O_3) was observed in the XRD pattern of pure Fe_2O_3 NPs. The NPs were crystalline in the rhombohedral lattice structure of α-Fe_2O_3 (JCPDS No. 24-0072), which had diffraction peaks at 2θ = 24.4°, 33.4°, 35.8°, 41.0°, 49.6°, 54.3°, 57.7°, 62.6°, 64.2°, 72.1°, 75.6°, 80.76°, 83.08°, 85.08°, and 89.10°, indexed as the (012), (104), (110), (113), (024), (116), (018), (214), (300), (1010), (217), (312), (0210), (134), and (126) planes [97]. The absence of secondary phases suggests that the produced material is pure and consists solely of the α-Fe_2O_3 single phase. The absence of any diffraction peak associated with the FeOOH phase suggests that the thermal annealing process entirely transformed the FeOOH into the α-Fe_2O_3 hematite phase. XRD investigations confirmed that the XRD patterns of α-Fe_2O_3-CeO_2 NC contain all the rhombohedral lattice structures of α-Fe_2O_3 and face-centered, cubic-structured CeO_2 NPs [98]. However, a slight reflection at around 35°, corresponding to the (110) plane of α-Fe_2O_3, was observed [96]. The majority of CeO_2 nanoparticles might be distributed on the surface of α-Fe_2O_3, effectively masking α-Fe_2O_3 and reducing its diffraction peaks in α-Fe_2O_3-CeO_2 NC, or the small amount of α-Fe_2O_3 NPs compared to CeO_2 in the nanocomposite [99].

Additionally, after gold deposition on the sample surface, additional peaks emerged at 38.2°, 44.4°, 64.6°, 77.6°, and 81.7° corresponding to the characteristic face-centered cubic (FCC) phase of gold (JCPDS no. 04-0784) [100]. The difference in their intensity reflected the strong supporting influence of gold dispersion on nanocomposite [101].

The average crystallite sizes (D) of the synthesized NPs and their NC were calculated based on the Debye Scherrer equation (Equation (2)):

$$D = \frac{K\lambda}{\beta \cos \theta} \quad (2)$$

where λ is X-ray wavelength (0.154 nm), K represents the shape factor (0.9), β is the full width at half maximum of the diffraction band (FWHM), and θ is the Bragg diffraction angle [102]. The calculated crystallite sizes of CeO_2, α-Fe_2O_3, α-Fe_2O_3-CeO_2, and α-Fe_2O_3-CeO_2@Au were 9.43 nm, 6.94 nm, 7.92 nm, and 36.42 nm, respectively. The NC modified with Au NPs obtained larger crystallite sizes than its pure form and components.

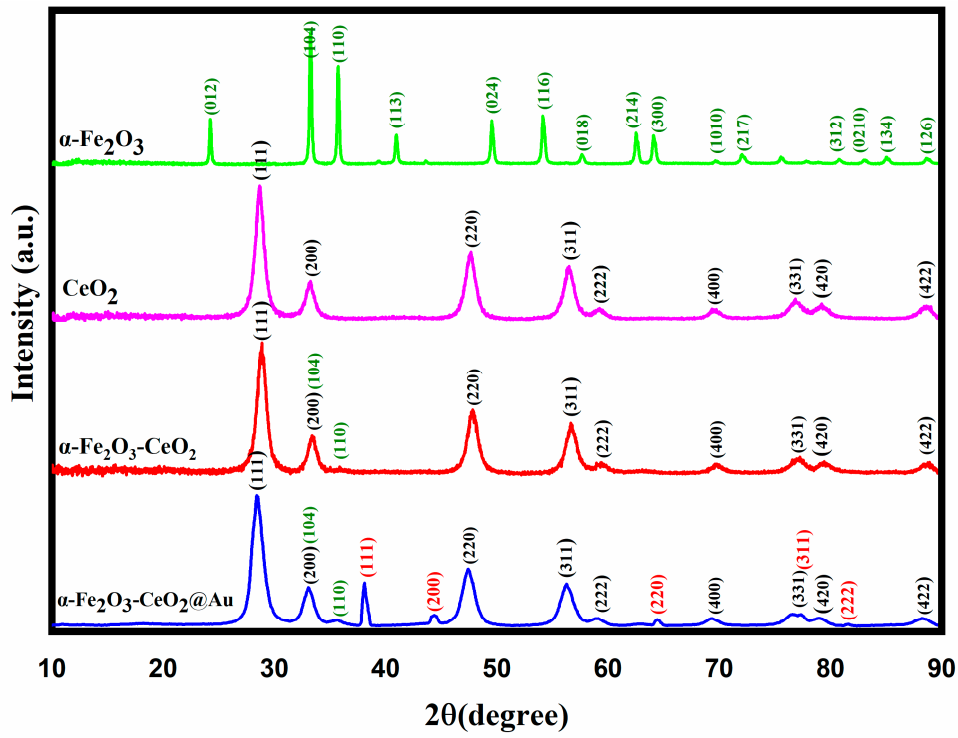

Figure 4. XRD patterns of α-Fe_2O_3, CeO_2, α-Fe_2O_3-CeO_2, and α-Fe_2O_3-CeO_2@Au.

3.4. XPS Analysis

The analysis using X-ray photoelectron spectroscopy (XPS) provides information about the chemical composition and oxidation state of elements (O, Ce, Fe, and Au) in α-Fe_2O_3-CeO_2@Au NC. Figure 5 provides high-resolution XPS spectra of Fe 2p, Ce 3d, O 1s, and Au 4f, along with the survey spectra of the NC. The survey spectrum in Figure 5a exhibits the peaks in binding energy associated with Ce $3d_{3/2}$, Ce $3d_{5/2}$, Fe $2p_{3/2}$, Fe $2p_{1/2}$, O 1s, C 1s, and Au 4f. There are two main peaks in the Fe 2p spectrum, located at 710.4 eV and 723.8 eV. These peaks correspond to Fe $2p_{3/2}$ and Fe $2p_{1/2}$, respectively, as well as two satellite peaks at 718.7 and 732.2 eV, which are attributed to Fe^3 (Figure 5b). This confirmed the presence of the standard Hematite phase in the α-Fe_2O_3-CeO_2@Au NC [103]. The Ce 3d spectrum shows Ce^{3+} and Ce^{4+} oxidation states associated with Ce $3d_{3/2}$ and Ce $3d_{5/2}$, suggesting the existence of the CeO_2 NPs in the NC. The Ce $3d_{5/2}$ peaks at 916.3, 897.9, and 888.4 eV mainly represent the vibration peaks of Ce^{4+}, indicating that the primary oxidation state of CeO_2 is Ce(IV). On the other hand, peaks at 907.1 and 900.4 eV belong to $Ce^{3+}3d_{3/2}$, and the ones at 882.0 eV refer to $Ce^{3+}3d_{3/2}$ (Figure 5c) [104,105].

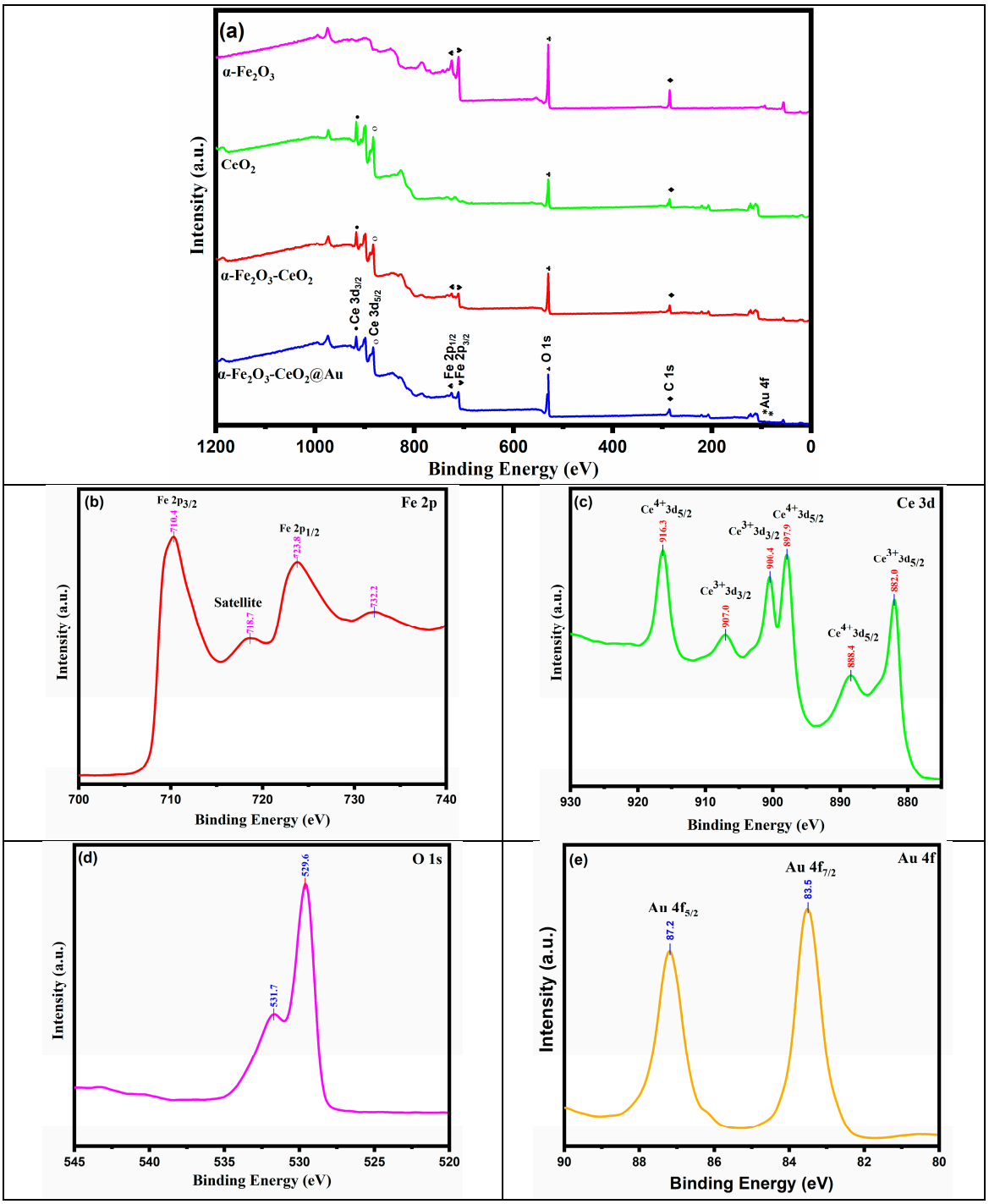

Figure 5. XPS spectra of α-Fe_2O_3-CeO_2@Au. (**a**) Survey spectrum of α-Fe_2O_3, CeO_2, α-Fe_2O_3-CeO_2, and α-Fe_2O_3-CeO_2@Au. High-resolution XPS spectra of (**b**) Fe 2p, (**c**) Ce 3d, (**d**) O 1s, and (**e**) Au 4f.

The O 1s spectrum demonstrated two broad peaks, with the lower binding energy peak (529.6 eV) assigned to the lattice oxygen of the metal oxide phase in CeO_2 NPs or Hematite and the higher binding energy peak (531.7 eV) corresponding to chemisorbed oxygen from hydroxyl (OH group) formed by oxygen (Figure 5d) [76,104]. The Au 4f XPS spectrum shows a doublet resulting from the spin-orbital splitting of $4f_{7/2}$ and $4f_{5/2}$ states, located at 83.6 eV and 87.2 eV, respectively, which is a typical characteristic of the presence of the Au NPs' state (Figure 5e) [100]. Two peaks were visible on the C 1s spectrum (Figure S1): one at 285 eV and the other at 288.4 eV. The first peak indicated sp^2-hybridized carbon

(C–C), while the second peak indicated O–C=O [104,106]. The XPS results confirmed the successful incorporation of the Hematite NPs into the CeO_2 NPs and the Au NPs, which aligns with the XRD and EDX results.

3.5. TEM Analysis

The surface morphology and the size of the α-Fe_2O_3, CeO_2, α-Fe_2O_3-CeO_2, and α-Fe_2O_3-CeO_2@Au NPs were investigated by TEM analysis, as depicted in Figure 6. The α-Fe_2O_3 NPs exhibited an irregular spherical and mixed-morphology nanostructure with an average particle size of approximately 6 nm, with some particles appearing larger due to agglomeration (Figure 6a). CeO_2 NPs displayed a fluorite structure, manifested as agglomerates of fine nanocrystallites with an average size of approximately 7 nm (Figure 6b). TEM images of α-Fe_2O_3-CeO_2 nanocomposites (Figure 6c) revealed the formation of large agglomerations of semi-spherical structures consisting of fine and large nanoparticles with a diameter of approximately 7 nm. These findings confirmed the formation of a heterostructure between α-Fe_2O_3 and CeO_2. Furthermore, the deposition of Au NPs on the nanocomposite surface did not disrupt the α-Fe_2O_3-CeO_2 nanostructure (Figure 6d), which indicates the successful integration of spherical AuNPs with the heterojunction to produce α-Fe_2O_3-CeO_2@Au, which might hinder the recombination of e^-–h^+ pairs and enhance their photocatalytic efficiency [40].

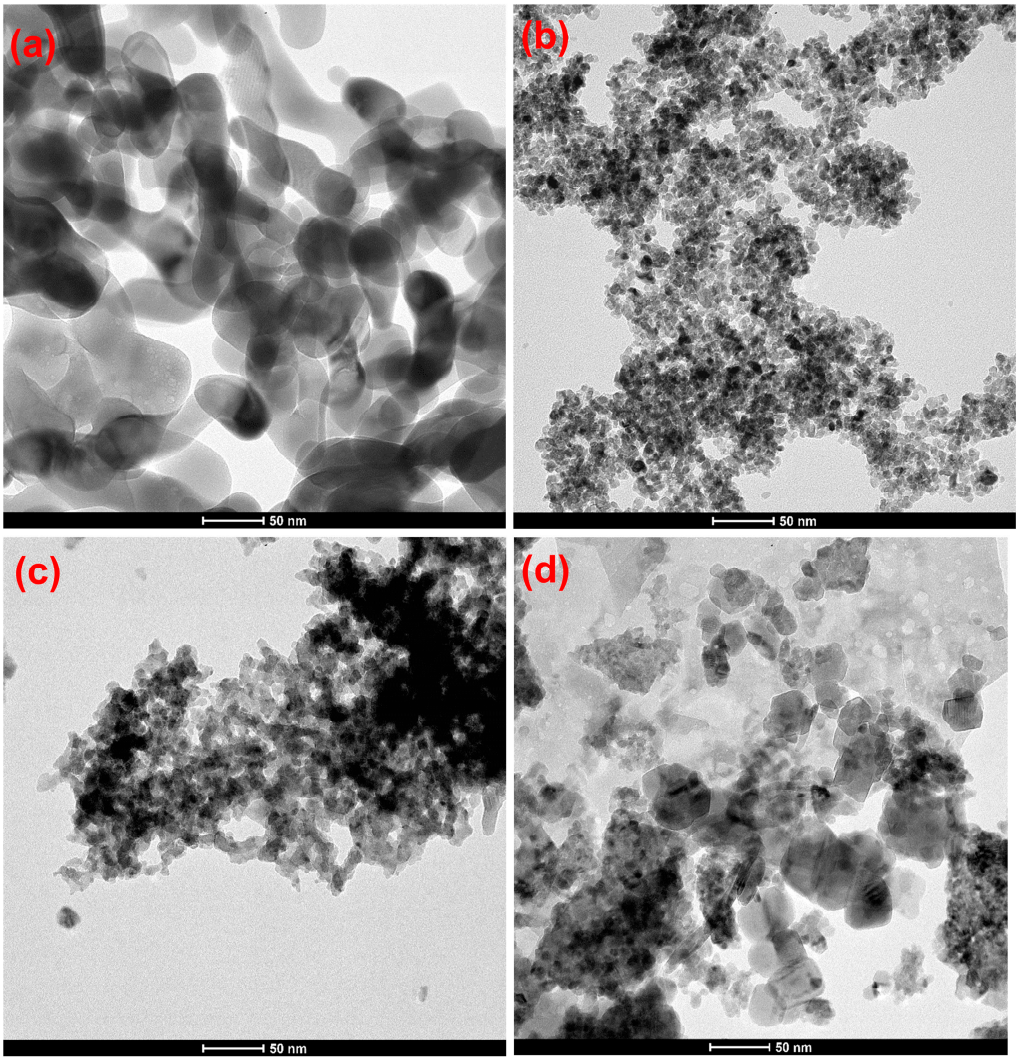

Figure 6. TEM images of (**a**) α-Fe_2O_3, (**b**) CeO_2, (**c**) α-Fe_2O_3-CeO_2, and (**d**) α-Fe_2O_3-CeO_2@Au.

3.6. SEM, Mapping, and EDX Analysis

The morphology and microstructure of α-Fe_2O_3, CeO_2, α-Fe_2O_3-CeO_2, and α-Fe_2O_3-CeO_2@Au were measured using SEM analysis, as represented in Figure 7. In Figure 7a, Hematite exhibits the aggregation of semi-spherical nanoparticles with a high-crystallinity nanostructure. Figure 7b displays CeO_2 NPs, which appear as an aggregation of semi-spherical fine nanoparticles. Meanwhile, the α-Fe_2O_3-CeO_2 nanocomposite exhibits the highest level of particle aggregation and showcases coral-like nanostructures with numerous vacancy defects on its surface. However, the original nanostructures of α-Fe_2O_3 NPs and CeO_2 NPs remained intact in the α-Fe_2O_3-CeO_2 NC, confirming the formation of a heterostructure between the two components (Figure 7c). Additionally, modifying α-Fe_2O_3 with CeO_2 NPs and Au NPs resulted in increased raggedness and surface rigidity (Figure 7d), while reducing particle aggregation. Consequently, the porosity of the surface increased, which facilitated greater contact between the active reactants. It is worth noting that this porous structure amplifies the surface area and creates additional pathways for charge carrier transfer, ultimately improving its photocatalytic activity [107].

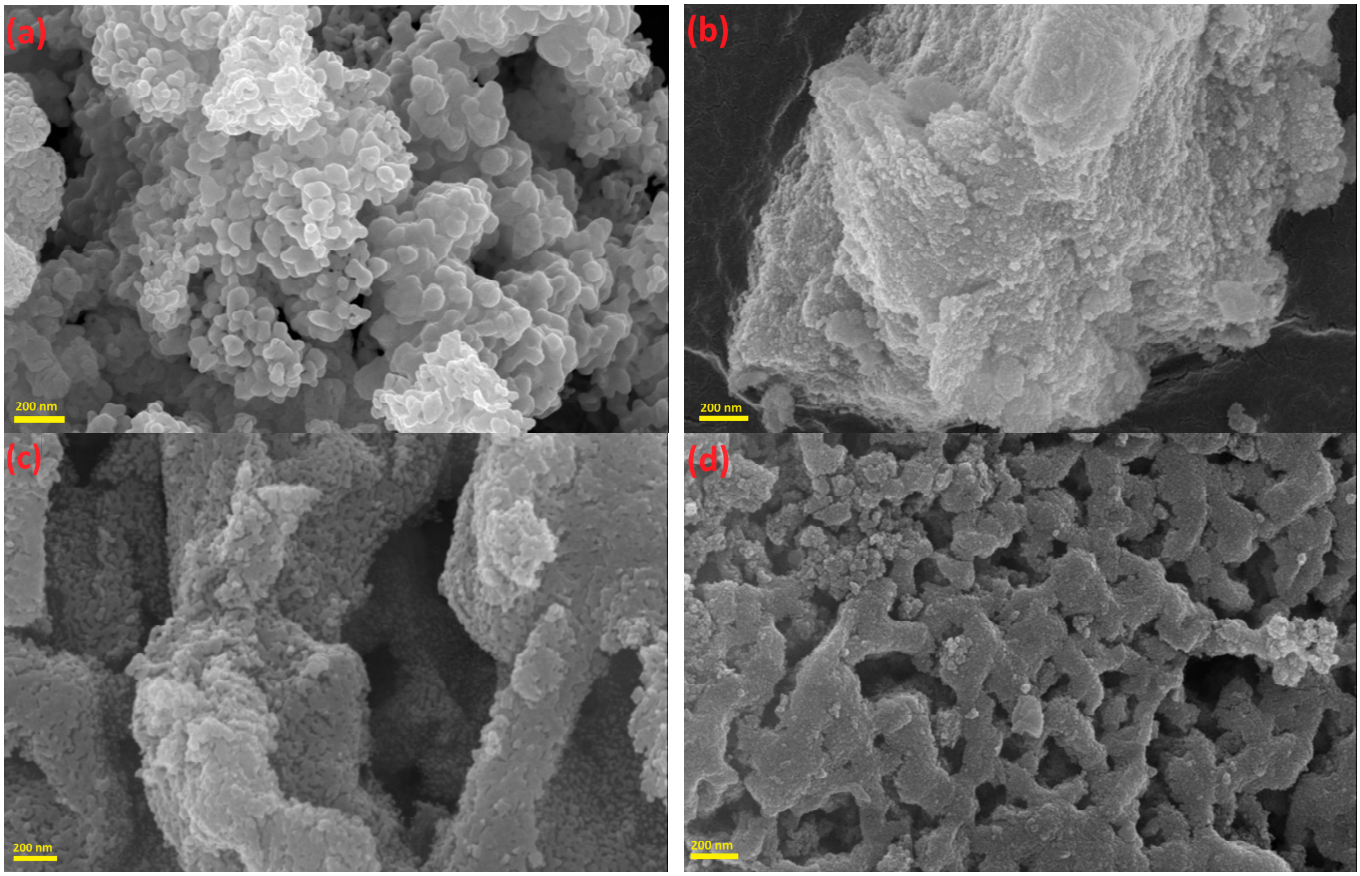

Figure 7. SEM images of (**a**) α-Fe_2O_3, (**b**) CeO_2, (**c**) α-Fe_2O_3-CeO_2, and (**d**) α-Fe_2O_3-CeO_2@Au.

Elemental mapping was utilized to confirm the steady distribution of elements on the α-Fe_2O_3-CeO_2@Au nanocomposite. The images (Figure S2b–e) demonstrated the homogeneous distribution of the primary constituent elements, namely Fe, Ce, and O, and the Au deposited on its surface. The nanocomposite's elemental composition was further investigated using energy-dispersive X-ray (EDX) spectra (Figure S2f). The absence of impurities and the presence of strong peaks attributed to Fe, Ce, O, and Au in the nanocomposite confirmed its successful formation. The spectrum indicated that the nanocomposite contained a significant amount of Fe, Ce, O, and Au. These findings were in line with the findings of the XRD and XPS tests. Element mapping indicates the uniform distribution of Fe, Ce, O, and Au species throughout the nanoparticle.

3.7. PL Analysis

Efficiently separating e^-–h^+ pairs is crucial in photocatalytic applications. Therefore, photoluminescence (PL) spectra were performed to assess the effectiveness of separating the photogenerated electrons and holes of α-Fe_2O_3-CeO_2 and α-Fe_2O_3-CeO_2@Au NCs. Figure S3 revealed that the α-Fe_2O_3-CeO_2 exhibited a prominent peak at 430 nm, attributed to the recombination of rapidly generated photoelectrons and holes. The intensity of the peak in α-Fe_2O_3-CeO_2@Au was diminished, likely due to the formation of a heterojunction between α-Fe_2O_3-CeO_2 and Au NPs, which can serve as an efficient electron sink. This suggests that the recombination of photogenerated electrons and holes was suppressed [90].

3.8. Photocatalytic Activity

Based on the bandgap and PL results, α-Fe_2O_3-CeO_2@Au NC was utilized for the efficient photodegradation of RB dye under the influence of visible-light irradiation, as shown in Figure 8. The desired concentrations of the photocatalyst and aqueous dye solution were stirred in the dark for 30 min at a neutral pH before being exposed to visible-light irradiation to achieve adsorption–desorption equilibrium. Under dark conditions, no significant degradation of RB was observed, with a high absorption peak at 546 nm. However, the spectrum decreased gradually in the presence of visible light. Figure 8 (Insert) displayed that the degradation rate gradually increased with increasing irradiation time, reaching 88.9% within 120 min. The increase in the photodegradation rate with a longer exposure time is caused by the heterojunction formed between α-Fe_2O_3 and CeO_2. This junction promotes the transfer of charge between the semiconductors. The SPR effect of Au NP_S improves the absorption of visible light by the heterojunction, resulting in the generation of more photoelectron–hole pairs. Additionally, the Au NPs can trap electrons and enhance the separation of electron–hole pairs, leading to the generation of more hydroxyl radicals. These radicals are responsible for degrading the dye [40,108].

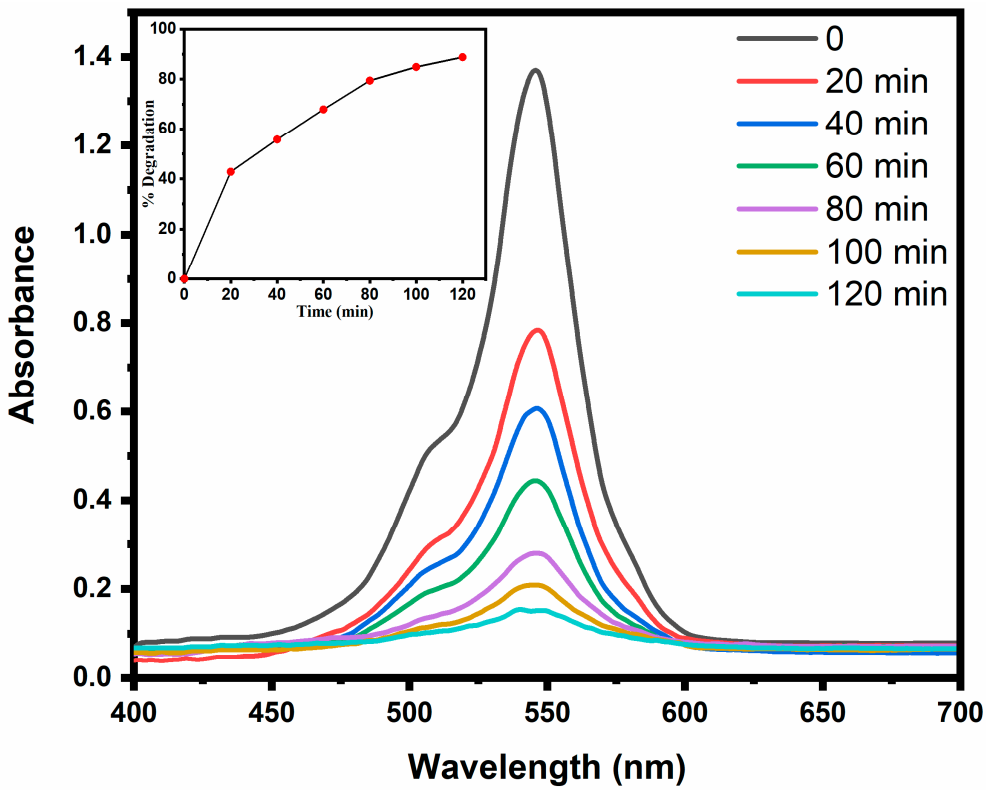

Figure 8. Time-dependent UV–Vis absorption spectra of the photocatalytic degradation of RB dye under visible-light irradiation (insert: % degradation plot). α-Fe_2O_3-CeO_2@Au nanocomposite (50 mg L^{-1}), RB dye (20 ppm), pH 7, and temperature 30 °C.

Furthermore, Table S1 compares the present photocatalytic activity of α-Fe_2O_3-CeO_2@Au NC with recent studies using Fe_2O_3-based nanoparticles under light irradiation [109–118].

3.9. Effect of Various Photocatalyst Concentrations

Optimizing the concentration of the α-Fe_2O_3-CeO_2@Au photocatalyst for the degradation of RB at a fixed pH, time, and temperature was the objective of a set of experiments that were carried out. The experiments involved different concentrations of the photocatalyst (20, 30, 40, 50 mg/L), as shown in Figure 9a. The results showed that as the concentration increased from 20 to 50 mg/L, the constant rate rose dramatically, from 0.00895 min^{-1} to 0.01789 min^{-1}. The highest degradation rate was achieved at a 50 mg/L catalyst concentration. With the increase in catalytic concentration, the availability of active sites increased, resulting in the rapid adsorption of dye molecules as compared to comparatively minor concentrations, thus reducing turbidity to opacity and enhancing the scattering of light radiation in the mixture solution. As a result, the passage of irradiation was enhanced, causing higher numeric values of photodegradation at 50 mg/L. This fact can also be attributed to the increased density of active sites and absorbed photons generating free hydroxy radicals ($^{\bullet}OH$) on the photocatalyst surface at a comparatively higher catalyst concentration, which led to the high photocatalytic degradation rate [119]. Therefore, 50 mg/L was selected as the optimum α-Fe_2O_3-CeO_2@Au concentration for further experiments for recovery cycle runs.

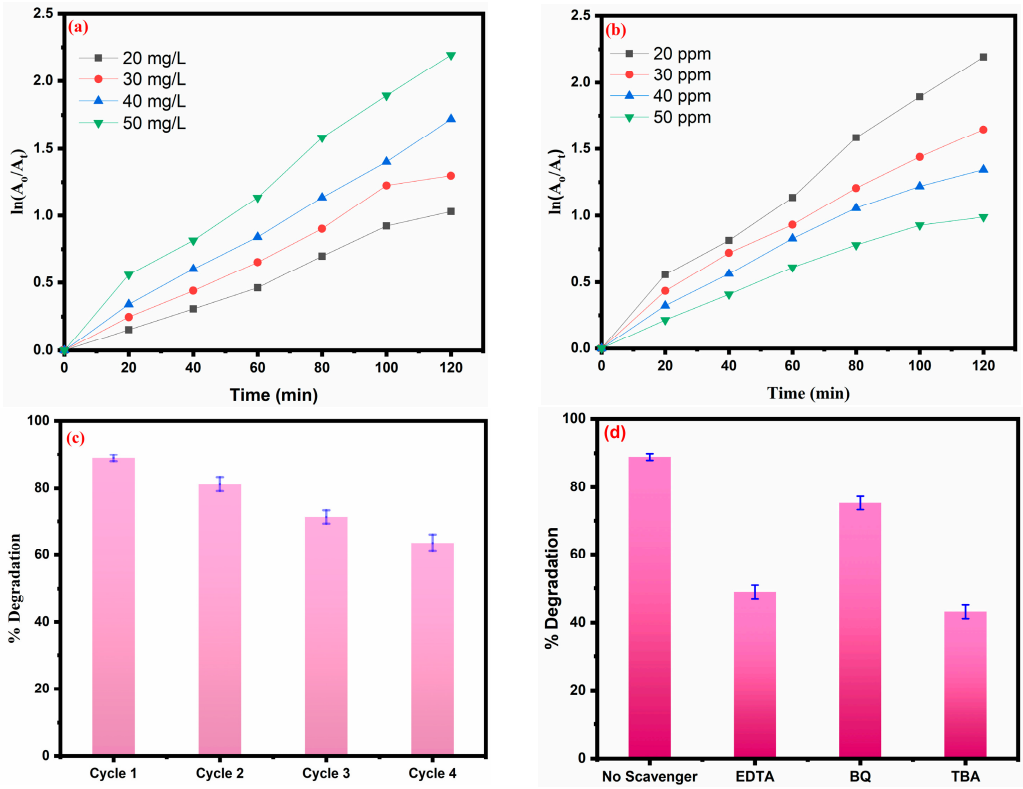

Figure 9. Kinetic curves analyzed by the pseudo-first-order kinetic model for the degradation of RB dye under visible-light irradiation for 120 min at a pH of 7 and 30 °C (**a**) using different concentrations of α-Fe_2O_3-CeO_2@Au (20 mg L^{-1}–50 mg L^{-1}) with a fixed amount of RB (20 ppm); (**b**) using different concentrations of RB dye (20 ppm–50 ppm) with a fixed amount of α-Fe_2O_3-CeO_2@Au (50 mg L^{-1}); (**c**) reusability of α-Fe_2O_3-CeO_2@Au for the photocatalytic degradation of RB dye removal under visible light for 120 min at a pH of 7 and 30 °C, and (**d**) scavenger effect on photocatalytic degradation using α-Fe_2O_3-CeO_2@Au (50 mg L^{-1}) for RB dye (20 ppm) removal under visible light for 120 min at a pH of 7 and 30 °C.

3.10. Effect of Various Dye Initial Concentrations

The influence of the initial concentration of RB on its photodegradation was examined using the α-Fe_2O_3-CeO_2@Au NC. The degradation rate was measured at a fixed amount of photocatalyst (50 mg/L), a neutral pH, and a temperature of 30 °C for 120 min. As the concentration of RB initially increased from 20 ppm to 50 ppm, the rate constant of the RB degradation declined from 0.01789 min^{-1} to 0.00851 min^{-1} (Figure 9b).

During the photodegradation process, increasing the initial concentrations of RB molecules promoted the interaction between active sites of α-Fe_2O_3-CeO_2@Au NC and RB molecules onto the surface, leading to enhanced turbidity and opacity. At elevated initial concentrations of RB molecules, the creation of electron–hole pairs decreased when exposed to light radiation with a constant catalytic concentration. Consequently, photodegradation efficiency is reduced. Overall, the photodegradation process involves the generation of reactive oxidation species (ROS) of $^{\bullet}OH$, h^+, $^{\bullet}O_2^-$ and e^-. Hence, a decline in ROS with increased RB concentrations at a fixed concentration of α-Fe_2O_3-CeO_2@Au NC was observed in this study. Additionally, the catalysts' surface quickly became saturated by dye molecules, leading to a shortage of active sites on which hydroxyl ions could adsorb. This results in a lower $^{\bullet}OH$ concentration, which, in turn, reduces the photodegradation efficiency, as the $^{\bullet}OH$'s contribution to the photo-degradation of dye molecules is significant [119]. Thus, we concluded that the comparatively lower concentration of RB, i.e., 20 ppm, is an optimum concentration for photodegradation in the presence of the α-Fe_2O_3-CeO_2@Au NC and light radiation. Table S2 presents the values of k (pseudo-first-order reaction rate constants) and half-lives for the photocatalytic degradation of RB using the α-Fe_2O_3-CeO_2@Au photocatalyst under different catalyst concentrations and initial concentrations.

3.11. Reusability Study

The collection and reusability of photocatalysts are crucial, and one highly effective approach to achieve this involves the utilization of magnetic materials [51]. In this study, α-Fe_2O_3 and CeO_2 were combined to form the α-Fe_2O_3-CeO_2@Au heterojunction, as hematite is the most suitable magnetic material due to its high magnetic properties, saturation magnetization, and coercivity [90]. The α-Fe_2O_3-CeO_2@Au NC showed excellent magnetic recyclability, as it could be rapidly isolated from the solution through the application of an external magnetic field. The photocatalyst stability was evaluated through 1–4 cycle experiments under visible-light irradiation (Figure 9c). After four cycles, the degradation of RB was observed to drop from 89% to 64% with less than a 25% decrease in its initial activity. After conducting four photocatalytic tests, the photodegradability of the catalyst decreased in comparison to the original photocatalyst owing to the degradation of the photocatalyst over time, which can cause a decrease in the efficiency the generation of reactive species. Additionally, the adsorption of the RB dye or other contaminants on the surface during the recycling process hindered the active sites of the photocatalyst's surface and reduced its photocatalytic activity [120]. This investigation indicates that the present photocatalyst can lead to the efficient photocatalytic degradation of RB dye due to its high photostability and confirms its reasonable catalytic reusability. To enhance the stability and reusability of the photocatalyst, it may be necessary to optimize or modify it without compromising its performance.

3.12. Effect of Radical Scavengers

To better understand the RB photocatalytic degradation process using α-Fe_2O_3-CeO_2@Au NC, a series of experiments were performed to deactivate potential reactive species by employing different scavengers for the purpose of radical scavenging (Figure 9d).

The experiments were performed under optimal conditions, which included an initial dye concentration of 20 ppm, a catalyst dose of 50 mg/L, a neutral pH, and an irradiation time of 120 min at 30 °C. To scavenge h^+, $^{\bullet}OH$, and $^{\bullet}O_2^-$, three chemical scavengers, namely ethylenediaminetetraacetic acid (EDTA; 0.5 mM), tert-butyl alcohol (TBA; 0.5 mM), and

benzoquinone (BQ; 0.5 mM), were used. There was also a control group without free radical scavengers. The results showed that EDTA, TBA, and BQ inhibited the reaction rate by approximately 40%, 46%, and 14%, respectively. The degradation effectiveness of RB exhibited a notable decrease upon the addition of TBA and EDTA. These findings indicated that $^{\bullet}OH$ and h^+ were the main reactive species contributing to the reaction process. This could be attributed to the hetero-junction formed between α-Fe_2O_3 and CeO_2, and the presence of deposited gold nanoparticles, which enhanced the charge transfer and, hence, electron–hole pair separation. On the other hand, the addition of BQ led to only a minor reduction in degradation efficiency, indicating that $^{\bullet}O_2^-$ did not play a significant role in the photocatalytic degradation despite its known involvement in the chain of heterogeneous/homogenous photocatalytic reactions [121]. This could be due to the consumption of superoxide radicals by other compounds present in the system, thereby reducing their overall impact on the degradation process [122]. Overall, the results suggested that $^{\bullet}OH$ and h^+ were the primary reactive species involved in RB degradation, while $^{\bullet}O_2^-$ had a low impact on the reaction process.

3.13. The Mechanism for Photodegrading RB Dye Using α-Fe_2O_3-CeO_2@Au NC

The photocatalytic technique has several distinguishing characteristics, such as specific bandgaps, as well as a specific surface area, morphology, reusability, and stability. In this study, a proposed photodegradation mechanism for RB dye by α-Fe_2O_3-CeO_2@Au heterojunction was presented based on the experimental results, as illustrated schematically in Figure 10. Upon exposure to visible light, photogenerated electrons in the valence bands (VB) of both CeO_2 and α-Fe_2O_3 were excited to their conduction bands (CB), leading to the generation of photogenerated holes in the valence bands. The CB of α-Fe_2O_3 (0.41 eV) is less negative than that of CeO_2 (−0.34). Therefore, the photogenerated electrons moved from CeO_2 to α-Fe_2O_3. Similarly, the VB of α-Fe_2O_3 is less positive (2.33 eV) than that of CeO_2 (2.46 eV). Hence, the photogenerated holes in CeO_2 also moved to α-Fe_2O_3. The creation of the Schottky barrier at the nanocomposite interface facilitated the charge transfer between the semiconductors [123]. In addition, under light irradiation, the surface plasmonic resonance (SPR) effect enhanced the efficiency of light absorption and resulted in the generation of additional photogenerated electron–hole pairs in the α-Fe_2O_3-CeO_2@Au nanocomposite [57,124]. However, the electrons accumulated on the CB of α-Fe_2O_3 cannot convert dissolved oxygen into $^{\bullet}O_2^-$ because the CB potential of α-Fe_2O_3 (0.41 eV) is less negative than the electrode potential of $O_2/^{\bullet}O_2^-$ (−0.33 eV vs. NHE). The SPR effect of Au NPs improved their ability to capture electrons, which assisted in separating the photogenerated electron–hole pairs and reduced the probability of recombination. Hence, the accumulated electrons on the CB of α-Fe_2O_3 can be easily trapped by Au NPs and then captured by the adsorbed O_2 to generate $^{\bullet}O_2^-$. This superoxide anion undergoes an additional reaction with water, leading to the generation of the highly reactive oxidizing agent, hydroxyl radical [122], which is consistent with the scavenger's findings. These transfers occurred much faster than the recombination of photogenerated electrons and holes in α-Fe_2O_3 [125]. The holes on VB of α-Fe_2O_3 reacted with OH^- to produce $^{\bullet}OH$, since the VB of α-Fe_2O_3 is more positive than the electrode potential of $^{\bullet}OH/H_2O$ (1.99 eV vs. NHE) [126]. The reactive oxidation species, including $^{\bullet}O_2^-$, $^{\bullet}OH$, and h^+, interacted with the RB molecules, contributing to their degradation [127]. In summary, the degradation process could be described by the following reaction:

$$\alpha\text{-}Fe_2O_3 + hv \rightarrow e^- \ (\alpha\text{-}Fe_2O_3) + h^+ \ (\alpha\text{-}Fe_2O_3) \quad (3)$$

$$CeO_2 + hv \rightarrow e^- \ (CeO_2) + h^+ \ (CeO_2) \quad (4)$$

$$e^- \ (CeO_2) \ CB \rightarrow e^- \ (\alpha\text{-}Fe_2O_3) \quad (5)$$

$$h^+ \ (CeO_2) \ VB \rightarrow h^+ \ (\alpha\text{-}Fe_2O_3) \quad (6)$$

$$e^- \ (\alpha\text{-}Fe_2O_3) \rightarrow e^- \ (Au^{\circ}) \quad (7)$$

$$e^- (Au^\circ) + O_2 \rightarrow {}^\bullet O_2^- \quad (8)$$

$$H_2O_2 + {}^\bullet O_2^- \rightarrow {}^\bullet OH \quad (9)$$

$$h^+ + (\alpha\text{-}Fe_2O_3) + OH^- \rightarrow {}^\bullet OH \quad (10)$$

$$\text{RB dye} + h^+ + {}^\bullet O_2^- + {}^\bullet OH \rightarrow H_2O + CO_2 \quad (11)$$

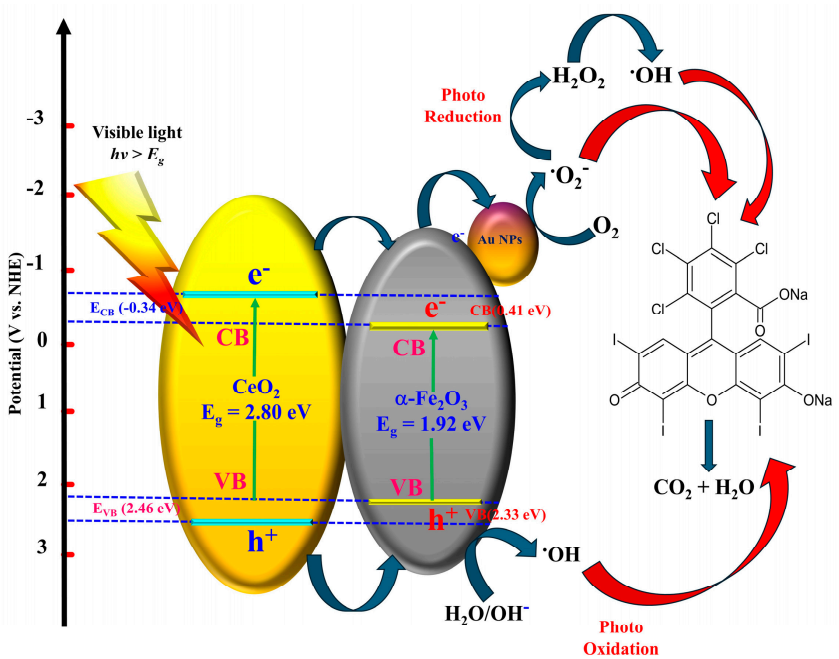

Figure 10. Photocatalytic mechanisms of α-Fe_2O_3-CeO_2@Au nanocomposite for the removal of Rose Bengal dye under visible-_light irradiation.

The band position of the as-synthesized samples was determined using empirical Equations (12) and (13).

$$E_{CB} = \chi - E_e - 0.5E_g \quad (12)$$

$$E_{VB} = E_{CB} + E_g \quad (13)$$

where χ is the electronegativity of the material and the χ values of CeO_2 and α-Fe_2O_3 were estimated previously to be 5.56 [128–130]; E_e is the energy of the free electrons on the hydrogen scale (4.5 eV); E_g represents the band gap of the material; E_{CB} stands for the conduction band potential; and E_{VB} denotes the valence band potential. The values of χ, E_g, E_{CB}, and E_{VB} for the synthesized samples are provided in Table S3.

4. Conclusions

A novel nanocomposite (NC) α-Fe_2O_3-CeO_2@Au was developed to efficiently eliminate Rose Bengal (RB) dye from wastewater using a photocatalytic technique under visible light. The NC was synthesized with stabilizing or capping agents, and the surface was coated with gold nanoparticles. The as-synthesized samples underwent characterizations of their structural, morphological, and optical properties. The study evaluated the effectiveness of α-Fe_2O_3-CeO_2@Au photocatalyst concentrations, initial dye concentration, and radical scavengers on the photocatalytic degradation of RB. The nanocomposite α-Fe_2O_3-CeO_2@Au (50 mg L^{-1}) achieved 88.9% for the removal of RB dye (20 ppm) in 120 min under visible-light irradiation at a pH of 7 and 30 °C. The results of the radical scavenging experiments suggested that holes (h^+) and hydroxyl radicals (•OH) were the main reactive species involved in the Rose Bengal degradation. The study highlights the potential of the nanocomposite for treating wastewater, especially for removing organic dyes. This composite can be easily separated using a magnetic field, offering an efficient method for

catalyst recovery and suggesting low operating expenses. However, the effectiveness of the composite decreases with repeated use, which raises sustainability concerns. To ensure the long-term sustainability of the photocatalytic treatment process, it is crucial to address the issues of catalyst stability and reusability.

Supplementary Materials: The following supporting information can be downloaded at: https://www.mdpi.com/article/10.3390/w16101334/s1, Figure S1: High-resolution XPS spectra of C 1s for α-Fe_2O_3-CeO_2@Au nanocomposite; Figure S2: (a) SEM image, Elemental mapping for (b) O atoms, (c) Fe atoms, (d), Ce atoms, and (e) Au atoms; and (f) Energy-dispersive X-ray (EDX) spectra analyses of α-Fe_2O_3-CeO_2@Au nanocomposite; Figure S3: PL (photoluminescence) spectra of α-Fe_2O_3-CeO_2 and α-Fe_2O_3-CeO_2@Au NCs; Table S1: Literature survey of Fe_2O_3-based heterojunction in photodegradation of toxic dyes; Table S2. Pseudo-first-order reaction rate constants (k) and half-lives for the photocatalytic degradation of RB by α-Fe_2O_3-CeO_2@Au photocatalyst at various catalyst concentrations and initial concentrations under visible light for 120 min at pH of 7 and 30 °C; Table S3: Estimated band gap (E_g), conduction band (E_{CB}), and valence band (E_{VB}) of as-synthesized samples.

Author Contributions: Conceptualization, M.A.M. and N.A.A.; methodology, M.A.M., R.P. and N.A.A.; software, M.A.M. and S.A.K.; validation, M.A.M., N.A.A. and S.A.K.; formal analysis, M.A.M. and N.A.A.; investigation, N.A.A.; resources, M.A.M., R.P. and S.A.K.; data curation, M.A.M. and S.A.K.; writing—original draft preparation, M.A.M. and N.A.A.; writing—review and editing, M.A.M., R.P. and S.A.K.; visualization, M.A.M., N.A.A., R.P. and S.A.K.; supervision, M.A.M. and S.A.K.; project administration, N.A.A.; funding acquisition, N.A.A. All authors have read and agreed to the published version of the manuscript.

Funding: This research was funded by the Deanship of Scientific Research (DSR), Northern Bor-der University, Arar, KSA, project number, (NBU-SAFIR-2024).

Data Availability Statement: The data can be found in the article.

Acknowledgments: The authors extend their appreciation to the Deanship of Scientific Research (DSR) at Northern Border University, Arar, KSA for funding this research work through project number NBU-SAFIR-2024.

Conflicts of Interest: The authors declare no conflicts of interest.

References

1. Shehnaz; Prasher, I.B.; Ahmad, N.; Ahmed, M.; Raghuwanshi, S.; Kumar, V.; Siddiqui, S.I.; Oh, S. Live Biomass of *Rigidoporus vinctus*: A Sustainable Method for Decoloration and Detoxification of Dyes in Water. *Microorganisms* **2023**, *11*, 1435. [CrossRef] [PubMed]
2. Siddiqui, S.I.; Allehyani, E.S.; Al-Harbi, S.A.; Hasan, Z.; Abomuti, M.A.; Rajor, H.K.; Oh, S. Investigation of Congo Red Toxicity towards Different Living Organisms: A Review. *Processes* **2023**, *11*, 807. [CrossRef]
3. Al-Tohamy, R.; Ali, S.S.; Li, F.; Okasha, K.M.; Mahmoud YA, G.; Elsamahy, T.; Sun, J. A critical review on the treatment of dye-containing wastewater: Ecotoxicological and health concerns of textile dyes and possible remediation approaches for environmental safety. *Ecotoxicol. Environ. Saf.* **2022**, *231*, 113160. [CrossRef] [PubMed]
4. Rathi, G.; Siddiqui, S.I.; Pham, Q. Nigella sativa seeds based antibacterial composites: A sustainable technology for water cleansing-A review. *Sustain. Chem. Pharm.* **2020**, *18*, 100332. [CrossRef]
5. Fatima, B.; Alwan, B.A.; Siddiqui, S.I.; Ahmad, R.; Almesfer, M.; Khanna, M.K.; Oh, S. Facile synthesis of cu-zn binary oxide coupled cadmium tungstate (Cu-znbo-cp-ct) with enhanced performance of dye adsorption. *Water* **2021**, *13*, 3287. [CrossRef]
6. Hassan, A.A.; Sajid, M.; Tanimu, A.; Abdulazeez, I.; Alhooshani, K. Removal of methylene blue and rose bengal dyes from aqueous solutions using 1-naphthylammonium tetrachloroferrate (III). *J. Mol. Liq.* **2021**, *322*, 114966. [CrossRef]
7. Hassan, S.S.; El-Shafie, A.S.; Zaher, N.; El-Azazy, M. Application of pineapple leaves as adsorbents for removal of rose bengal from wastewater: Process optimization operating face-centered central composite design (FCCCD). *Molecules* **2020**, *25*, 3752. [CrossRef] [PubMed]
8. Siddiqui, S.I.; Chaudhry, S.A. Arsenic: Toxic effects and remediation. In *Advanced Materials for Wastewater Treatment*; Wiley Online Library: Hoboken, NJ, USA, 2017; pp. 1–27.
9. Sztandera, K.; Gorzkiewicz, M.; Zizzi, E.A.; Dybczak, N.; Poltorak, L.; Deriu, M.A.; Klajnert-Maculewicz, B. Cellular Uptake of Rose Bengal Is Mediated by OATP1B1/1B3 Transporters. *Bioelectrochemistry* **2023**, *152*, 108449. [CrossRef] [PubMed]
10. Demartis, S.; Obinu, A.; Gavini, E.; Giunchedi, P.; Rassu, G. Nanotechnology-based rose Bengal: A broad-spectrum biomedical tool. *Dye. Pigment.* **2021**, *188*, 109236. [CrossRef]

11. Kaur, J.; Singhal, S. Heterogeneous photocatalytic degradation of rose bengal: Effect of operational parameters. *Phys. B Condens. Matter* **2014**, *450*, 49–53. [CrossRef]
12. Rauf, M.A.; Marzouki, N.; Körbahti, B.K. Photolytic decolorization of Rose Bengal by UV/H_2O_2 and data optimization using response surface method. *J. Hazard. Mater.* **2008**, *159*, 602–609. [CrossRef] [PubMed]
13. Siddiqui, S.I.; Chaudhry, S.A. Green adsorbents from plant sources for the removal of arsenic: An emerging wastewater treatment technology. In *Plant-Based Natural Products: Derivatives and Applications*; Wiley Online Library: Hoboken, NJ, USA, 2017; pp. 193–215.
14. Nguyen, H.T.; Siddiqui, S.I.; Maeng, S.K.; Oh, S. Biological detoxification of oxytetracycline using Achromobacter-immobilized bioremediation system. *J. Water Process Eng.* **2023**, *52*, 103491. [CrossRef]
15. Khasim, S.; Dastager, S.G.; Alahmdi, M.I.; Hamdalla, T.A.; Ulla, M.F.; Panneerselvam, C.; Makandar, M.B. Green synthesis of multifunctional Cu/MnO@ Biochar 3D structure as a high-performance anode material in Li-ion batteries and oxidative removal of Cango-red dye. *Case Stud. Chem. Environ. Eng.* **2024**, *9*, 100561. [CrossRef]
16. Ye, Q.; Wu, H.; Li, J.; Huang, Y.; Zhang, M.; Yi, Q.; Yan, B. Preparation of 1,8-dichloroanthraquinone/graphene oxide/poly (vinylidene fluoride) (1,8-AQ/GO/PVDF) mediator membrane and its application to catalyzing biodegradation of azo dyes. *Ecotoxicol. Environ. Saf.* **2023**, *268*, 115681. [CrossRef] [PubMed]
17. Choudhry, A.; Sharma, A.; Siddiqui, S.I.; Ahamad, I.; Sajid, M.; Khan, T.A.; Chaudhry, S.A. Origanum vulgare manganese ferrite nanocomposite: An advanced multifunctional hybrid material for dye remediation. *Environ. Res.* **2023**, *220*, 115193. [CrossRef]
18. GC., S.S.; Alkanad, K.; Hezam, A.; Alsalme, A.; Al-Zaqri, N.; Lokanath, N.K. Enhanced photo-Fenton activity over a sunlight-driven ignition synthesized α-Fe_2O_3-Fe_3O_4/CeO_2 heterojunction catalyst enriched with oxygen vacancies. *J. Mol. Liquids* **2021**, *335*, 116186.
19. Fatima, B.; Siddiqui, S.I.; Rajor, H.K.; Malik, M.A.; Narasimharao, K.; Ahmad, R.; Kim, K.H. Photocatalytic removal of organic dye using green synthesized zinc oxide coupled cadmium tungstate nanocomposite under natural solar light irradiation. *Environ. Res.* **2023**, *216*, 114534. [CrossRef] [PubMed]
20. de Oliveira Guidolin, T.; Possolli, N.M.; Polla, M.B.; Wermuth, T.B.; de Oliveira, T.F.; Eller, S.; Cechinel, M.A.P. Photocatalytic pathway on the degradation of methylene blue from aqueous solutions using magnetite nanoparticles. *J. Clean. Prod.* **2021**, *318*, 128556. [CrossRef]
21. Fatima, B.; Siddiqui, S.I.; Ahmad, R.; Linh NT, T.; Thai, V.N. CuO-ZnO-$CdWO_4$: A sustainable and environmentally benign photocatalytic system for water cleansing. *Environ. Sci. Pollut. Res.* **2021**, *28*, 53793–53803. [CrossRef]
22. Waheed, I.F.; Thayee Al-Janaby, O.Y.; Foot, P.J.S. Novel $MgFe_2O_4$-CuO/GO heterojunction magnetic nanocomposite: Synthesis, characterization, and batch photocatalytic degradation of methylene blue dye. *J. Mol. Liquids* **2022**, *357*, 119084. [CrossRef]
23. Matussin, S.N.; Khan, F.; Harunsani, M.H.; Kim, Y.M.; Khan, M.M. Visible-light-induced photocatalytic and photoantibacterial activities of Co-Doped CeO_2. *ACS Omega* **2023**, *8*, 11868–11879. [CrossRef]
24. Alzahrani, E.A.; Nabi, A.; Kamli, M.R.; Albukhari, S.M.; Althabaiti, S.A.; Al-Harbi, S.A.; Malik, M.A. Facile Green Synthesis of ZnO NPs and Plasmonic Ag-Supported ZnO Nanocomposite for Photocatalytic Degradation of Methylene Blue. *Water* **2023**, *15*, 384. [CrossRef]
25. Alghamdi, Y.G.; Krishnakumar, B.; Malik, M.A.; Alhayyani, S. Design and preparation of biomass-derived activated carbon loaded TiO_2 photocatalyst for photocatalytic degradation of reactive red 120 and ofloxacin. *Polymers* **2022**, *14*, 880. [CrossRef]
26. Malika, M.; Sonawane, S.S. The sono-photocatalytic performance of a Fe_2O_3 coated TiO_2 based hybrid nanofluid under visible light via RSM. *Colloids Surf. A* **2022**, *641*, 128545. [CrossRef]
27. Dewangan, K.; Singh, D.; Satpute, N.; Singh, R.; Jaiswal, A.; Shrivas, K.; Bahadur, I. Hydrothermally grown α-MoO_3 microfibers for photocatalytic degradation of methylene blue dye. *J. Mol. Liquids* **2022**, *349*, 118202. [CrossRef]
28. Chen, Q.; Wu, L.; Zhao, X.; Yang, X.-J. Fabrication of Zn-Ti layered double oxide nanosheets with ZnO/$ZnTiO_3$ heterojunction for enhanced photocatalytic degradation of MO, RhB and MB. *J. Mol. Liquids* **2022**, *353*, 118794. [CrossRef]
29. Alzahrani, S.A.; Al-Thabaiti, S.A.; Al-Arjan, W.S.; Malik, M.A.; Khan, Z. Preparation of ultra long α-MnO_2 and Ag@MnO_2 nanoparticles by seedless approach and their photocatalytic performance. *J. Mol. Struct.* **2017**, *1137*, 495–505. [CrossRef]
30. Yu, Z.; Liu, X.; Liu, Y.; Li, Y.; Zhang, Z.; Chen, K.; Han, S. Synergetic Catalysis of Ni@C@CeO_2 for Driving Ab/Desorption of MgH2 at Moderate Temperature. *Fuel* **2024**, *357*, 129726. [CrossRef]
31. Shabna, S.; Dhas, S.S.J.; Biju, C.S. Potential progress in SnO_2 nanostructures for enhancing photocatalytic degradation of organic pollutants. *Catal. Commun.* **2023**, *177*, 106642. [CrossRef]
32. Shao, P.; Ren, Z.; Tian, J.; Gao, S.; Luo, X.; Shi, W.; Cui, F. Silica hydrogel-mediated dissolution-recrystallization strategy for synthesis of ultrathin α-Fe_2O_3 nanosheets with highly exposed (110) facets: A superior photocatalyst for degradation of bisphenol S. *Chem. Eng. J.* **2017**, *323*, 64–73. [CrossRef]
33. Li, Y.; Liu, K.; Zhang, J.; Yang, J.; Huang, Y.; Tong, Y. Engineering the band-edge of Fe_2O_3/ZnO nanoplates via separate dual cation incorporation for efficient photocatalytic performance. *Ind. Eng. Chem. Res.* **2020**, *59*, 18865–18872. [CrossRef]
34. Singh, S.; Kumar, A.; Kataria, N.; Kumar, S.; Kumar, P. Photocatalytic activity of α-Fe_2O_3@ CeO_2 and CeO_2@ α-Fe_2O_3 core-shell nanoparticles for degradation of Rose Bengal dye. *J. Environ. Chem. Eng.* **2021**, *9*, 106266.
35. Rasouli, K.; Alamdari, A.; Sabbaghi, S. Ultrasonic-assisted synthesis of α-Fe_2O_3@TiO_2 photocatalyst: Optimization of effective factors in the fabrication of photocatalyst and removal of non-biodegradable cefixime via response surface methodology-central composite design. *Sep. Purif. Technol.* **2023**, *307*, 122799. [CrossRef]

36. Harijan, D.K.; Gupta, S.; Ben, S.K.; Srivastava, A.; Singh, J.; Chandra, V. High photocatalytic efficiency of α-Fe_2O_3-ZnO composite using solar energy for methylene blue degradation. *Phys. B Condens. Matter* **2022**, *627*, 413567. [CrossRef]
37. Devi, L.G.; Shyamala, R. Photocatalytic activity of SnO_2–α-Fe_2O_3 composite mixtures: Exploration of number of active sites, turnover number and turnover frequency. *Mater. Chem. Front.* **2018**, *2*, 796–806. [CrossRef]
38. Althabaiti, S.A.; Khan, Z.; Bawaked, S.M.; Al-Sheheri, S.Z.; Mokhtar, M.; Malik, M.A.; Narasimharao, K. PtOx deposited Fe_3O_4-ZnO/TiO_2 nanocomposites for photocatalytic H_2 production under visible light. *J. Environ. Chem. Eng.* **2023**, *11*, 110615. [CrossRef]
39. Albeladi, A.; Khan, Z.; Al-Thabaiti, S.A.; Patel, R.; Malik, M.A.; Mehta, S. Fe_3O_4-CdO Nanocomposite for Organic Dye Photocatalytic Degradation: Synthesis and Characterization. *Catalysts* **2024**, *14*, 71. [CrossRef]
40. Lin, C.H.; Chen, Y.C.; Hsu, P.K.; Gloter, A.; Huang, W.H.; Chen, C.L.; Chen, S.Y. Enhanced Photocatalytic Performance of TiO_2@CeO_2 Hollow Structure through Synergetic Surface and Interface Engineering. *Adv. Sustain. Syst.* **2023**, *7*, 2300230. [CrossRef]
41. Alzahrani, K.A.; Ismail, A.A. α-Fe_2O_3/CeO_2 S-Scheme Heterojunction Photocatalyst for Enhanced Photocatalytic H_2 Evolution. *Surf. Interfaces* **2023**, *39*, 102935. [CrossRef]
42. Tambat, S.; Umale, S.; Sontakke, S. Photocatalytic degradation of Milling Yellow dye using sol–gel synthesized CeO_2. *Mater. Res. Bull.* **2016**, *76*, 466–472. [CrossRef]
43. Malekkiani, M.; Ravari, F.; Heshmati Jannat Magham, A.; Dadmehr, M.; Groiss, H.; Hosseini, H.A.; Sharif, R. Fabrication of Graphene-Based TiO_2@ CeO_2 and CeO_2@ TiO_2 Core–Shell Heterostructures for Enhanced Photocatalytic Activity and Cytotoxicity. *ACS Omega* **2022**, *7*, 30601–30621. [CrossRef] [PubMed]
44. Ji, R.; Zhu, Z.; Ma, W.; Tang, X.; Liu, Y.; Huo, P. A heterojunction photocatalyst constructed by the modification of 2D-CeO_2 on 2D-MoS_2 nanosheets with enhanced degrading activity. *Catal. Sci. Technol.* **2020**, *10*, 788–800. [CrossRef]
45. Channei, D.; Chansaenpak, K.; Jannoey, P.; Phanichphant, S. The staggered heterojunction of CeO_2/CdS nanocomposite for enhanced photocatalytic activity. *Solid State Sci.* **2019**, *96*, 105951. [CrossRef]
46. Sahoo, S.K.; Mohapatra, M.; Pandey, B.; Verma, H.C.; Das, R.P.; Anand, S. Preparation and Characterization of α-Fe_2O_3–CeO_2 Composite. *Mater. Charact.* **2009**, *60*, 425–431. [CrossRef]
47. Aboutaleba, W.A.; Gobaraa, H.M.; Hashima, K.M.; Heneina, S.A.; Hassanb, S.A. The catalytic performance of Fe_2O_3-CeO_2 nanocomposite in ethanol conversion. *Egypt. J. Chem.* **2016**, *59*, 445–463.
48. Mazloum-Ardakani, M.; Sabaghian, F.; Yavari, M.; Ebady, A.; Sahraie, N. Enhance the performance of iron oxide nanoparticles in supercapacitor applications through internal contact of α-Fe_2O_3@ CeO_2 core-shell. *J. Alloys Compd.* **2020**, *819*, 152949. [CrossRef]
49. Zheng, X.; Huang, M.; You, Y.; Peng, H.; Wen, J. Core-shell structured α-Fe_2O_3@ CeO_2 heterojunction for the enhanced visible-light photocatalytic activity. *Mater. Res. Bull.* **2018**, *101*, 20–28. [CrossRef]
50. Jawhari, A.H.; Hasan, N.; Radini, I.A.; Narasimharao, K.; Malik, M.A. Noble metals deposited $LaMnO_3$ nanocomposites for photocatalytic H_2 production. *Nanomaterials* **2022**, *12*, 2985. [CrossRef]
51. Jawhari, A.H.; Hasan, N.; Radini, I.A.; Malik, M.A.; Narasimharao, K. Pt-Ag/Ag_3PO_4-WO_3 nanocomposites for photocatalytic H_2 production from bioethanol. *Fuel* **2023**, *344*, 127998. [CrossRef]
52. Al Thabaiti, S.A.; Khan, Z.; Al-Thubaiti, K.S.; Bawaked, S.M.; Al-Sheheri, S.Z.; Mokhtar, M.; Narasimharao, K. Au-Deposited Ce0. 5Zr0. 5O2 Nanostructures for Photocatalytic H2 Production under Visible Light. *Catalysts* **2023**, *13*, 1340. [CrossRef]
53. Tada, H.; Fujishima, M.; Naya, S.I. Fundamentals and Applications of Gold Nanoparticle-Based Plasmonic Photocatalysts for Water Purification. *ACS ES&T Eng.* **2024**, *4*, 506–524.
54. Zhu, H.; Yuan, X.; Yao, Q.; Xie, J. Shining photocatalysis by gold-based nanomaterials. *Nano Energy* **2021**, *88*, 106306. [CrossRef]
55. Dinçer, C.A.; Yıldız, N.; Aydoğan, N.; Çalımlı, A. A comparative study of Fe_3O_4 nanoparticles modified with different silane compounds. *Appl. Surf. Sci.* **2014**, *318*, 297–304. [CrossRef]
56. Komeily-Nia, Z.; Montazer, M.; Latifi, M. Synthesis of nano copper/nylon composite using ascorbic acid and CTAB. *Colloids Surf. A* **2013**, *439*, 167–175. [CrossRef]
57. Ahire, J.H.; Wang, Q.; Coxon, P.R.; Malhotra, G.; Brydson, R.; Chen, R.; Chao, Y. Highly luminescent and nontoxic amine-capped nanoparticles from porous silicon: Synthesis and their use in biomedical imaging. *ACS Appl. Mater. Interfaces* **2012**, *4*, 3285–3292. [CrossRef] [PubMed]
58. Marcelo, G.A.; Lodeiro, C.; Capelo, J.L.; Lorenzo, J.; Oliveira, E. Magnetic, fluorescent and hybrid nanoparticles: From synthesis to application in biosystems. *Mater. Sci. Eng. C* **2020**, *106*, 110104. [CrossRef]
59. Gopannagari, M.; Kumar, D.P.; Park, H.; Kim, E.H.; Bhavani, P.; Reddy, D.A.; Kim, T.K. Influence of surface-functionalized multi-walled carbon nanotubes on CdS nanohybrids for effective photocatalytic hydrogen production. *Appl. Catal. B Environ.* **2018**, *236*, 294–303. [CrossRef]
60. Guo, S.; Duan, J.A.; Qian, D.; Tang, Y.; Wu, D.; Su, S.; Zhao, Y. Content variations of triterpenic acid, nucleoside, nucleobase, and sugar in jujube (*Ziziphus jujuba*) fruit during ripening. *Food Chem.* **2015**, *167*, 468–474. [CrossRef] [PubMed]
61. Yuan, C.G.; Huo, C.; Gui, B.; Liu, J.F.; Chen, Y.S. Facile phyto-mediated synthesis of silver nanoparticles using Chinese winter jujube (*Ziziphus jujuba* Mill. cv. Dongzao) extract and their antibacterial/catalytic properties. *IET Nanobiotechnol.* **2017**, *11*, 973–980. [CrossRef]
62. Tahergorabi, Z.; Abedini, M.R.; Mitra, M.; Fard, M.H.; Beydokhti, H. Ziziphus jujuba: A red fruit with promising anticancer activities. *Pharmacogn. Rev.* **2015**, *9*, 99.

63. Dave, S.; Das, J.; Shah, M.P. *Photocatalytic Degradation of Dyes: Current Trends and Future Perspectives*; Elsevier: Amsterdam, The Netherlands, 2021.
64. Adhikari, S.P.; Hood, Z.D.; More, K.L.; Chen, V.W.; Lachgar, A. A Visible-Light-Active Heterojunction with Enhanced Photocatalytic Hydrogen Generation. *ChemSusChem* **2016**, *9*, 1869–1879. [CrossRef]
65. Tomar, L.J.; Chakrabarty, B.S. Synthesis, structural and optical properties of TiO_2-ZrO_2 nanocomposite by hydrothermal method. *Adv. Mater. Lett.* **2013**, *4*, 64–67. [CrossRef]
66. Sari, E.O.; Fadli, A.; Amri, A. The 3 hours-hydrothermal synthesis of high surface area superparamagnetic Fe_3O_4 core-shell nanoparticles. *J. Sains Materi Indones.* **2018**, *19*, 9–13. [CrossRef]
67. Sobhani, A. Hydrothermal synthesis of $CuMn_2O_4$/CuO nanocomposite without capping agent and study its photocatalytic activity for elimination of dye pollution. *Int. J. Hydrogen Energy* **2022**, *47*, 20138–20152. [CrossRef]
68. Ramesh, A.M.; Gangadhar, A.; Chikkamadaiah, M.; Shivanna, S. Hydrothermal synthesis of Ga_2O_3/TiO_2 nanocomposites with highly enhanced solar photocatalysis and their biological interest. *J. Photochem. Photobiol.* **2021**, *6*, 100020. [CrossRef]
69. Golmohammadi, M.; Honarmand, M.; Ghanbari, S. A Green Approach to Synthesis of ZnO Nanoparticles Using Jujube Fruit Extract and Their Application in Photocatalytic Degradation of Organic Dyes. *Spectrochim. Acta Part A* **2020**, *229*, 117961. [CrossRef]
70. Naikoo, G.A.; Mustaqeem, M.; Hassan, I.U.; Awan, T.; Arshad, F.; Salim, H.; Qurashi, A. Bioinspired and green synthesis of nanoparticles from plant extracts with antiviral and antimicrobial properties: A critical review. *J. Saudi Chem. Soc.* **2021**, *25*, 101304. [CrossRef]
71. Murugadoss, G.; Kumar, D.D.; Kumar, M.R.; Venkatesh, N.; Sakthivel, P. Silver Decorated CeO_2 Nanoparticles for Rapid Photocatalytic Degradation of Textile Rose Bengal Dye. *Sci. Rep.* **2021**, *11*, 1080. [CrossRef] [PubMed]
72. Malini, B.; Raj, G.A.G. C, N and S-Doped TiO_2-Characterization and Photocatalytic Performance for Rose Bengal Dye Degradation under Daylight. *J. Environ. Chem. Eng.* **2018**, *6*, 5763–5770. [CrossRef]
73. Isai, K.A.; Shrivastava, V.S. Photocatalytic Degradation of Methylene Blue Using ZnO and 2% Fe–ZnO Semiconductor Nanomaterials Synthesized by Sol–Gel Method: A Comparative Study. *SN Appl. Sci.* **2019**, *1*, 1247. [CrossRef]
74. Adel, G.; Javad, M.; Amiri, M.S.; Mohammad, M.; Alireza, H.; Aliakbar, H.; Iriti, M. Resveratrol-mediated gold-nanoceria synthesis as green nanomedicine for phytotherapy of hepatocellular carcinoma. *Front. Biosci.* **2022**, *27*, 227.
75. Peng, Y.; Chen, Q.G.; Wang, D.; Zhou, H.Y.; Xu, A.W. Synthesis of one-dimensional WO3–Bi2WO6 heterojunctions with enhanced photocatalytic activity. *CrystEngComm* **2015**, *17*, 569–576. [CrossRef]
76. Li, Q.; Antony, R.P.; Wong, L.H.; Ng, D.H. Promotional effects of cetyltrimethylammonium bromide surface modification on a hematite photoanode for photoelectrochemical water splitting. *RSC Adv.* **2015**, *5*, 100142–100146. [CrossRef]
77. Gnanam, S.; Rajendran, V. Influence of various surfactants on size, morphology, and optical properties of CeO_2 nanostructures via facile hydrothermal route. *J. Nanopart.* **2013**, *2013*, 839391. [CrossRef]
78. Li, L.; Xu, Y.; Zhong, D.; Zhong, N. CTAB-surface-functionalized magnetic MOF@ MOF composite adsorbent for Cr (VI) efficient removal from aqueous solution. *Colloids Surf. A* **2020**, *586*, 124255. [CrossRef]
79. Hssaini, L.; Razouk, R.; Bouslihim, Y. Rapid prediction of fig phenolic acids and flavonoids using mid-infrared spectroscopy combined with partial least square regression. *Front. Plant Sci.* **2022**, *13*, 429. [CrossRef]
80. Aldughaylibi, F.S.; Raza, M.A.; Naeem, S.; Rafi, H.; Alam, M.W.; Souayeh, B.; Mir, T.A. Extraction of bioactive compounds for antioxidant, antimicrobial, and antidiabetic applications. *Molecules* **2022**, *27*, 5935. [CrossRef]
81. Zhu, Z.; Huo, P.; Lu, Z.; Yan, Y.; Liu, Z.; Shi, W.; Dong, H. Fabrication of magnetically recoverable photocatalysts using g-C3N4 for effective separation of charge carriers through like-Z-scheme mechanism with Fe_3O_4 mediator. *Chem. Eng. J.* **2018**, *331*, 615–625. [CrossRef]
82. Warsi, M.F.; Shaheen, N.; Sarwar, M.I.; Agboola, P.O.; Shakir, I.; Zulfiqar, S. A comparative study on photocatalytic activities of various transition metal oxides nanoparticles synthesized by wet chemical route. *Desalin. Water Treat.* **2021**, *211*, 181–195. [CrossRef]
83. Zhang, L.; Yang, Y.; Li, Y.; Wu, J.; Wu, S.; Tan, X.; Hu, Q. Highly efficient UV-visible-infrared photothermocatalytic removal of ethyl acetate over a nanocomposite of CeO_2 and Ce-doped manganese oxide. *Chin. J. Catal.* **2022**, *43*, 379–390. [CrossRef]
84. Sabouri, Z.; Sabouri, M.; Amiri, M.S.; Khatami, M.; Darroudi, M. Plant-based synthesis of cerium oxide nanoparticles using Rheum turkestanicum extract and evaluation of their cytotoxicity and photocatalytic properties. *Mater. Technol.* **2022**, *37*, 555–568. [CrossRef]
85. Rajendran, A.; Alsawalha, M.; Alomayri, T. Biogenic synthesis of husked rice-shaped iron oxide nanoparticles using coconut pulp (Cocos nucifera L.) extract for photocatalytic degradation of Rhodamine B dye and their in vitro antibacterial and anticancer activity. *J. Saudi Chem. Soc.* **2021**, *25*, 101307. [CrossRef]
86. Parthasarathy, V.; Selvi, J.; Senthil Kumar, P.; Anbarasan, R.; Mahalakshmi, S. Evaluation of mechanical, optical and thermal properties of PVA nanocomposites embedded with Fe_2O_3 nanofillers and the investigation of their thermal decomposition characteristics under non-isothermal heating condition. *Polym. Bull.* **2021**, *78*, 2191–2210. [CrossRef]
87. He, Y.P.; Miao, Y.M.; Li, C.R.; Wang, S.Q.; Cao, L.; Xie, S.S.; Burda, C. Size and structure effect on optical transitions of iron oxide nanocrystals. *Phys. Rev. B* **2005**, *71*, 125411. [CrossRef]
88. Han, Q.; Zhang, D.; Guo, J.; Zhu, B.; Huang, W.; Zhang, S. Improved catalytic performance of Au/α-Fe_2O_3-like-worm catalyst for low temperature CO oxidation. *Nanomaterials* **2019**, *9*, 1118. [CrossRef] [PubMed]

89. Subashini, A.; Prasath, P.V.; Sagadevan, S.; Lett, J.A.; Fatimah, I.; Mohammad, F.; Oh, W.C. Enhanced photocatalytic degradation efficiency of graphitic carbon nitride-loaded CeO_2 nanoparticles. *Chem. Phys. Lett.* **2021**, *769*, 138441. [CrossRef]
90. Shi, Z.; Zhang, Y.; Shen, X.; Duoerkun, G.; Zhu, B.; Zhang, L.; Chen, Z. Fabrication of g-C_3N_4/BiOBr heterojunctions on carbon fibers as weaveable photocatalyst for degrading tetracycline hydrochloride under visible light. *Chem. Eng. J.* **2020**, *386*, 124010. [CrossRef]
91. Carrot, G.; Valmalette, J.C.; Plummer CJ, G.; Scholz, S.M.; Dutta, J.; Hofmann, H.; Hilborn, J.G. Gold nanoparticle synthesis in graft copolymer micelles. *Colloid Polym. Sci.* **1998**, *276*, 853–859. [CrossRef]
92. Narasimharao, K.; Al-Shehri, A.; Al-Thabaiti, S. Porous Ag–Fe_2O_3 Nanocomposite Catalysts for the Oxidation of Carbon Monoxide. *Appl. Catal. A* **2015**, *505*, 431–440. [CrossRef]
93. Ahmad, A.; Javed, M.S.; Khan, S.; Almutairi, T.M.; Mohammed, A.A.; Luque, R. Green synthesized Ag decorated CeO_2 nanoparticles: Efficient photocatalysts and potential antibacterial agents. *Chemosphere* **2023**, *310*, 136841. [CrossRef]
94. Cordero-García, M.X.; Rojas-García, E.; Salinas-Rodríguez, E.; Gómez, S.A. Influence on pretreatment in CeO_2 and Au/CeO_2 nanocomposite to improve the creation of surface defects enabling modification in optical interband. *Rev. Mex. De Ing. Química* **2023**, *22*, Mat2991. [CrossRef]
95. Gobara, H.M.; Abouta leb, W.A.; Hashem, K.M.; Hassan, S.A.; Henein, S.A. A novel route for synthesis of α-Fe_2O_3–CeO_2 nanocomposites for ethanol conversion. *J. Mater. Sci.* **2017**, *52*, 550–568. [CrossRef]
96. Li, J.; Lu, Y.; Li, D.; Ma, L.; Qi, F.; Yu, L. Semiconductor heterostructure composite materials of Fe_2O_3 and CeO_2 for low-temperature solid oxide fuel cells. *J. Mater. Sci. Mater. Electron.* **2020**, *31*, 11825–11832. [CrossRef]
97. Jayababu, N.; Poloju, M.; Shruthi, J.; Reddy MV, R. Ultrasensitive resistivity-based ethanol sensor based on the use of CeO_2-Fe_2O_3 core-shell microclusters. *Microchim. Acta.* **2019**, *186*, 712. [CrossRef] [PubMed]
98. Han, R.; Li, W.; Pan, W.; Zhu, M.; Zhou, D.; Li, F.S. 1D magnetic materials of Fe_3O_4 and Fe with high performance of microwave absorption fabricated by electrospinning method. *Sci. Rep.* **2014**, *4*, 7493. [CrossRef] [PubMed]
99. Geng, G.; Chen, P.; Guan, B.; Liu, Y.; Yang, C.; Wang, N.; Liu, M. Sheetlike gold nanostructures/graphene oxide composites via a one-pot green fabrication protocol and their interesting two-stage catalytic behaviors. *RSC Adv.* **2017**, *7*, 51838–51846. [CrossRef]
100. Ren, X.; Song, Y.; Liu, A.; Zhang, J.; Yang, P.; Zhang, J.; Yuan, G.; An, M.; Osgood, H.; Wu, G. Role of polyethyleneimine as an additive in cyanide-free electrolytes for gold electrodeposition. *RSC Adv.* **2015**, *5*, 64806–64813. [CrossRef]
101. Tabakova, T.; Avgouropoulos, G.; Papavasiliou, J.; Manzoli, M.; Boccuzzi, F.; Tenchev, K.; Ioannides, T. CO-free hydrogen production over Au/CeO_2–Fe_2O_3 catalysts: Part 1. Impact of the support composition on the performance for the preferential CO oxidation reaction. *Appl. Catal. B Environ.* **2011**, *101*, 256–265. [CrossRef]
102. Cao, Y.; Zhao, Y.; Wang, Y.; Zhang, Y.; Wen, J.; Zhao, Z.; Zhu, L. Reduction degree regulated room-temperature terahertz direct detection based on fully suspended and low-temperature thermally reduced graphene oxides. *Carbon* **2019**, *144*, 193–201. [CrossRef]
103. Arul, N.S.; Mangalaraj, D.; Ramachandran, R.; Grace, A.N.; Han, J.I. Fabrication of CeO_2/Fe_2O_3 composite nanospindles for enhanced visible light driven photocatalysts and supercapacitor electrodes. *J. Mater. Chem. A* **2015**, *3*, 15248–15258. [CrossRef]
104. Lykaki, M.; Stefa, S.; Carabineiro, S.A.; Pandis, P.K.; Stathopoulos, V.N.; Konsolakis, M. Facet-dependent reactivity of Fe_2O_3/CeO_2 nanocomposites: Effect of ceria morphology on CO oxidation. *Catalysts* **2019**, *9*, 371. [CrossRef]
105. Xing, Y.; Wu, Y.; Li, L.; Shi, Q.; Shi, J.; Yun, S.; Akbar, M.; Wang, B.; Kim, J.-S.; Zhu, B. Proton shuttles in CeO_2/$CeO_{2-\delta}$ core–shell structure. *ACS Energy Lett.* **2019**, *4*, 2601–2607. [CrossRef]
106. Jayachandiran, J.; Arivanandhan, M.; Padmaraj, O.; Jayavel, R.; Nedumaran, D. Investigation on Ozone-Sensing Characteristics of Surface Sensitive Hybrid rGO/WO3 Nanocomposite Films at Ambient Temperature. *Adv. Compos. Hybrid Mater.* **2020**, *3*, 16–30. [CrossRef]
107. Zhao, X.; Wu, P.; Lu, D.; Fang, P.; Liu, M.; Qian, Z. Synergistic effect of Fe_2O_3 and CeO_2 co-modified titanate nanosheet heterojunction on enhanced photocatalytic degradation. *J. Nanopart. Res.* **2017**, *19*, 325. [CrossRef]
108. Lee, S.Y.; Kang, D.; Jeong, S.; Do, H.T.; Kim, J.H. Photocatalytic degradation of rhodamine B dye by TiO_2 and gold nanoparticles supported on a floating porous polydimethylsiloxane sponge under ultraviolet and visible light irradiation. *ACS Omega* **2020**, *5*, 4233–4241. [CrossRef] [PubMed]
109. Zaman, F.u.; Xie, B.; Zhang, J.; Gong, T.; Cui, K.; Hou, L.; Xu, J.; Zhai, Z.; Yuan, C. MOFs Derived Hetero-ZnO/Fe_2O_3 Nanoflowers with Enhanced Photocatalytic Performance towards Efficient Degradation of Organic Dyes. *Nanomaterials* **2021**, *11*, 3239. [CrossRef] [PubMed]
110. Rouibah, K.; Akika, F.Z.; Rouibah, C.; Boudermine, H.R.; Douafer, S.; Boukerche, S.; Boukerche, G.; Benamira, M. Solar Photocatalytic Degradation of Methyl Green on $CuFe_2O_4$/α Fe_2O_3 Heterojunction. *Inorg. Chem. Commun.* **2023**, *148*, 110361. [CrossRef]
111. Sharma, K.; Sudhaik, A.; Raizada, P.; Thakur, P.; Pham, X.M.; Van Le, Q.; Nguyen, V.-H.; Ahamad, T.; Thakur, S.; Singh, P. Constructing α-Fe_2O_3/g-C_3N_4/SiO_2 S-Scheme-Based Heterostructure for Photo-Fenton-like Degradation of Rhodamine B Dye in Aqueous Solution. *Environ. Sci. Pollut. Res.* **2023**, *30*, 124902–124920. [CrossRef]
112. Bagheri, F.; Chaibakhsh, N. Efficient Visible-Light Photocatalytic Ozonation for Dye Degradation Using Fe_2O_3/MoS_2 Nanocomposite. *Sep. Sci. Technol.* **2021**, *56*, 3022–3032. [CrossRef]
113. Khurram, R.; Nisa, Z.U.; Javed, A.; Wang, Z.; Hussien, M.A. Synthesis and Characterization of an α-Fe_2O_3-Decorated g-C_3N_4 Heterostructure for the Photocatalytic Removal of MO. *Molecules* **2022**, *27*, 1442. [CrossRef]

114. Vignesh, S.; Suganthi, S.; Srinivasan, M.; Tamilmani, A.; Sundar, J.K.; Gedi, S.; Palanivel, B.; Shaikh, S.F.; Ubaidullah, M.; Raza, M.K. Investigation of Heterojunction between α-Fe_2O_3/V_2O_5 and g-C_3N_4 Ternary Nanocomposites for Upgraded Photo-degradation Performance of Mixed Pollutants: Efficient Dual Z-scheme Mechanism. *J. Alloys Compd.* **2022**, *902*, 163705. [CrossRef]
115. Helmiyati, H.; Fitriana, N.; Chaerani, M.L.; Dini, F.W. Green Hybrid Photocatalyst Containing Cellulose and γ–Fe_2O_3–ZrO_2 Heterojunction for Improved Visible-Light Driven Degradation of Congo Red. *Opt. Mater.* **2022**, *124*, 111982. [CrossRef]
116. Mukhtar, F.; Munawar, T.; Nadeem, M.S.; ur Rehman, M.N.; Khan, S.A.; Koc, M.; Batool, S.; Hasan, M.; Iqbal, F. Dual Z-Scheme Core-Shell PANI-CeO_2-Fe_2O_3-NiO Heterostructured Nanocomposite for Dyes Remediation under Sunlight and Bacterial Disinfection. *Environ. Res.* **2022**, *215*, 114140. [CrossRef]
117. Kumar, P.; Kumar, U.; Huang, Y.-C.; Tsai, P.-Y.; Liu, C.-H.; Wu, C.-H.; Huang, W.-M.; Chen, K.-L. Photocatalytic Activity of a Hydrothermally Synthesized γ-Fe_2O_3@Au/MoS_2 Heterostructure for Organic Dye Degradation under Green Light. *J. Photochem. Photobiol. A Chem.* **2022**, *433*, 114186. [CrossRef]
118. Yahia, B.; Faouzi, S.; Mohamed, T. Methylene Blue Photo-degradation on the Hetero-junction System α-$Fe_2O_3/BaTiO_3$ under Sunlight. *J. Photochem. Photobiol. A Chem.* **2023**, *439*, 114634. [CrossRef]
119. Razavi, F.S.; Ghanbari, D.; Salavati-Niasari, M. Comparative study on the role of noble metal nanoparticles (Pt and Pd) on the photocatalytic performance of the $BaFe_{12}O_{19}/TiO_2$ magnetic nanocomposite: Green synthesis, characterization, and removal of organic dyes under visible light. *Ind. Eng. Chem. Res.* **2022**, *61*, 13314–13327. [CrossRef]
120. Mohamad Idris, N.H.; Rajakumar, J.; Cheong, K.Y.; Kennedy, B.J.; Ohno, T.; Yamakata, A.; Lee, H.L. Titanium dioxide/polyvinyl alcohol/cork nanocomposite: A floating photocatalyst for the degradation of methylene blue under irradiation of a visible light source. *ACS Omega* **2021**, *6*, 14493–14503. [CrossRef] [PubMed]
121. Hayyan, M.; Hashim, M.A.; AlNashef, I.M. Superoxide Ion: Generation and Chemical Implications. *Chem. Rev.* **2016**, *116*, 3029–3085. [CrossRef] [PubMed]
122. Saeed, M.; Usman, M.; Haq, A.U. *Catalytic Degradation of Organic Dyes in Aqueous Medium*; IntechOpen: London, UK, 2018; Volume 13, p. 197.
123. Othman, Z.; Sinopoli, A.; Mackey, H.R.; Mahmoud, K.A. Efficient Photocatalytic Degradation of Organic Dyes by AgNPs/TiO_2/Ti_3C_2Tx MXene Composites under UV and Solar Light. *ACS Omega* **2021**, *6*, 33325–33338. [CrossRef]
124. Wu, J.; Luo, C.; Li, D.; Fu, Q.; Pan, C. Preparation of Au nanoparticle-decorated ZnO/NiO heterostructure via nonsolvent method for high-performance photocatalysis. *J. Mater. Sci.* **2017**, *52*, 1285–1295. [CrossRef]
125. Parvari, R.; Ghorbani-Shahna, F.; Bahrami, A.; Azizian, S.; Assari, M.J.; Farhadian, M. α-Fe_2O_3/Ag/gC_3N_4 Core-Discontinuous Shell Nanocomposite as an Indirect Z-Scheme Photocatalyst for Degradation of Ethylbenzene in the Air Under White LEDs Irradiation. *Catal. Lett.* **2020**, *150*, 3455–3469. [CrossRef]
126. Huang, L.; Liu, J.; Li, Y.; Yang, L.; Wang, C.; Liu, J.; Huang, L. Enhancement of photocatalytic activity of Z-scheme BiO2-x/BiOI heterojunction through vacancy engineering. *Appl. Surf. Sci.* **2021**, *555*, 149665. [CrossRef]
127. Pang, Y.L.; Lim, S.; Ong, H.C.; Chong, W.T. Research progress on iron oxide-based magnetic materials: Synthesis techniques and photocatalytic applications. *Ceram. Int.* **2016**, *42*, 9–34. [CrossRef]
128. Xu, Y.; Schoonen, M.A. The absolute energy positions of conduction and valence bands of selected semiconducting minerals. *Am. Mineral.* **2000**, *85*, 543–556. [CrossRef]
129. Channei, D.; Chansaenpak, K.; Phanichphant, S.; Jannoey, P.; Khanitchaidecha, W.; Nakaruk, A. Synthesis and characterization of WO_3/CeO_2 heterostructured nanoparticles for photodegradation of indigo carmine dye. *ACS Omega* **2021**, *6*, 19771–19777. [CrossRef]
130. Gao, Y.; Ma, H.; Han, C.; Gui, C.; Deng, C. Preparation of Ag_3PO_4/α-Fe_2O_3 hybrid powders and their visible light catalytic performances. *RSC Adv.* **2022**, *12*, 6328–6335. [CrossRef]

Disclaimer/Publisher's Note: The statements, opinions and data contained in all publications are solely those of the individual author(s) and contributor(s) and not of MDPI and/or the editor(s). MDPI and/or the editor(s) disclaim responsibility for any injury to people or property resulting from any ideas, methods, instructions or products referred to in the content.